日本磁気学会
ISSN 2432-0250
Journal of the Magnetics Society of Japan
Electronic Journal URL: https://www.jstage.jst.go.jp/browse/msjmag

Vol.41 No.5　2017

Journal

JOURNAL OF THE MAGNETICS SOCIETY OF JAPAN

Vol.41 No.5 2017

日本磁気学会

ISSN 2432-0250

HP: http://www.magnetics.jp/ e-mail: msj@bj.wakwak.com
Electronic Journal: http://www.jstage.jst.go.jp/browse/msjmag

Physicist
Peter Grünberg

未来をどこまで想像できるか。

進みつづける時間の先に、何を見るか。
止まることのない時間の向こうに、何を思い描くか。
想像したことのない未来は、創造できない。
まっすぐな視線の先にしか、新しい常識は現れない。
先駆的なアイデアだって、革新的なテクノロジーだって、
それは、未来を自由に想像し、未来を強く渇望し、
そこに向かおうとするひたむきな意志からしか生まれない。
未来とは、前を向く者だけに与えられる、
現在という時間からのかけがえのない贈り物だ。
だから、未来に夢を見よう。未来に絵を描こう。
この世界の未来を、どこまでも想像しよう。

www.attractingtomorrow.tdk.co.jp

Attracting Tomorrow TDK

世界初！
高温超電導型VSM

新製品

世界初*、高温超電導マグネットをVSMに採用することで
測定速度 当社従来機1/20を実現。
0.5mm cube磁石のBr, HcJ高精度測定が可能と
なりました。
*2014年7月 東英工業調べ

測定結果例

高温超電導VSMによるNdFeB(sint.) 0.5mm cube BHカーブ

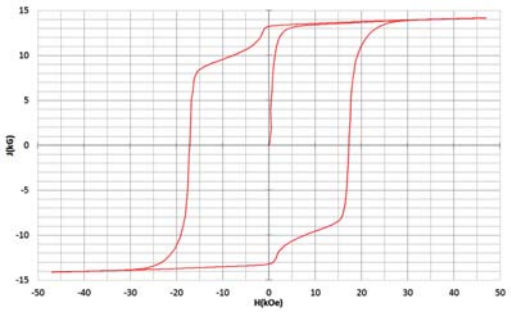

磁化測定レンジ：0.2emu
Br = 13.2kG　　HcJ = 17.2kOe

高温超電導VSMによるNdFeB(sint.) 1mm cube BHカーブ

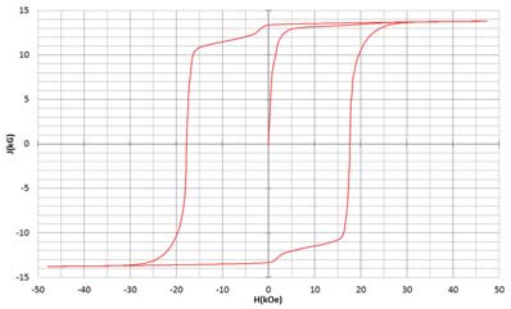

磁化測定レンジ：2emu
Br = 13.3kG　　HcJ = 17.7kOe

高温超電導VSMによるNdFeB(sint.) 4mm cube BHカーブ

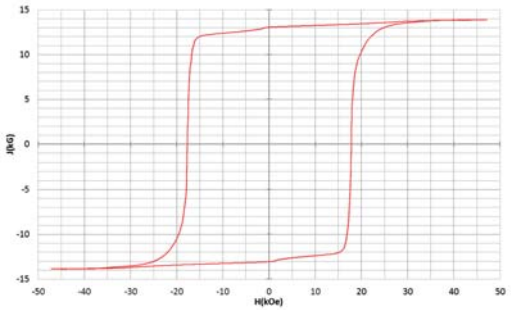

磁化測定レンジ：100emu
Br = 13.1kG　　HcJ = 17.8kOe

高速測定を実現

高温超電導マグネット採用により、高速測定を実現しました。Hmax= 5Tesla, Full Loop 測定が2分で可能です。
（当社従来機：Full Loop測定　40分）

小試料のBr,HcJ高精度測定

0.5mm cube 磁石のBr,HcJ高精度測定ができ、表面改質領域を切り出しBr,HcJの強度分布等、微小変化量の比較測定が可能です。
また、試料の加工劣化の比較測定が可能です。

試料温度可変測定

−50℃～+200℃温度可変UNIT（オプション）

磁界発生部の小型化

マグネットシステム部寸法：0.8m×0.3m×0.3m

TOEI 東英工業株式会社
http://www.toeikogyo.co.jp
〒194-0035 東京都町田市忠生1-8-13
TEL：042-791-1211 FAX：042-792-0490
E-mail : sales@toeikogyo.co.jp

有限要素法解析ソフトウェア COMSOL Multiphysics®

COMSOL MULTIPHYSICS®

マルチフィジックスの進化論

無制限・強連成で実現象に即したシミュレーション事例のご紹介

永久磁石を利用した磁気軸受の解析例

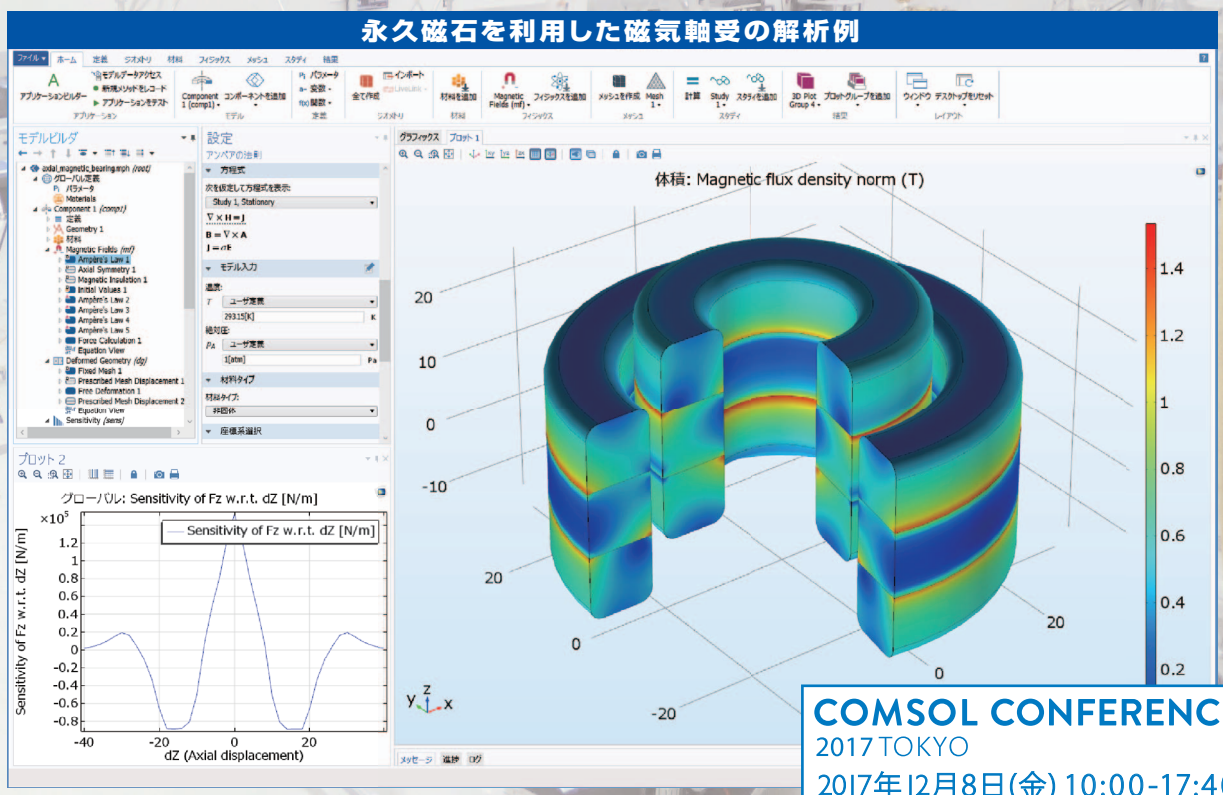

COMSOL CONFERENCE
2017 TOKYO
2017年12月8日(金) 10:00-17:40
秋葉原UDXビル4F (UDX Gallery/Next)
http://www.kesco.co.jp/conference/

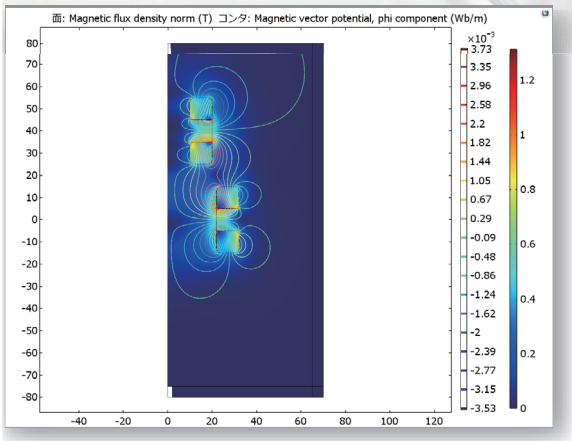

永久磁石を使用した磁気軸受

永久磁石を使用した軸受はターボ機械、ポンプ、モータ、発電機やフライホイール式エネルギー貯蔵システムなど、様々な分野で使用されています。非接触かつ潤滑不要で保守整備を大幅に省略できる点は、従来の機械式ベアリングと比べて重要なメリットです。
この例では、軸方向の永久磁石軸受の磁気力と剛性などの設計パラメータを計算する方法を示しています。

※AC/DCモジュールはCOMSOL Multiphysicsと併用するアドオン製品です。

AC/DC モジュールの適用例

- AC/DC 電流分布、電場分布
- バイオヒーティング
- コイルとソレノイド
- SPICE 回路とフィールドシミュレーション
- 接触抵抗
- 電磁両立性 (EMC) および電磁妨害 (EMI)
- 電磁力およびトルク
- 電磁力シールド
- 電気機械の変形
- ホール効果を利用したセンサ
- インシュレータ、コンデンサ、誘電体
- モータ、ジェネレータ、および他の電気機械
- 非線形材料
- 寄生容量とインダクタンス
- 永久磁石と電磁石
- 多孔質材料
- 抵抗および誘導加熱
- センサ
- 超伝導体
- 変圧器とインダクタ

COMSOL Multiphysics® なら、今まで不可能だった3種以上のマルチフィジックス解析を強連成で実現できます。30日間全機能無料トライアル、無料の導入セミナー、1000種を超える世界の様々な事例をご提供いたします。詳しくは、下記の弊社営業部までお問い合せください。

COMSOL
http://www.comsol.jp

KESCO KEISOKU ENGINEERING SYSTEM
計測エンジニアリングシステム株式会社
http://www.kesco.co.jp/comsol/
Tel : 03-5282-7040 ・ Fax : 03-5282-0808

新製品

磁区観察ユニット

既存のプローバ装置で磁区観察を！
小型でシンプル！磁区観察をより手軽に！

※概要・特徴

- プローバ装置などに取り付けることが可能な小型・低価格の磁区観察ユニット
- 面内 / 垂直どちらの磁化方向にも対応
- 社内設計光学系による面内磁区の高コントラスト観察（空間分解能 3μm 以下 ）
- 光学系ヘッドの大きさは、 150×150×300mm 重量も 2kg と軽量・コンパクト
- 白色 LED 光源を用いた高安定性・長寿命
- オプションとして顕微鏡スタンド・ステージ・高機能観察 / 解析ソフトウェアなどを用意

※観察例

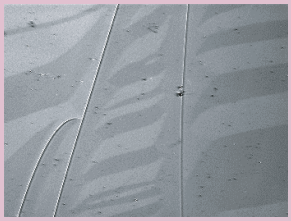

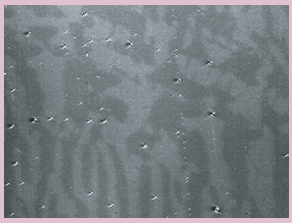

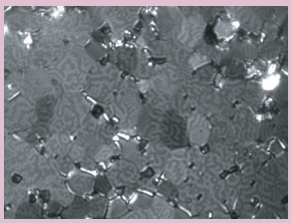

※オプション例

- θ-X-Y-Z 軸ステージ
- 顕微鏡スタンド

※この組み合わせでも重量は約 9kg ですので、 設置場所を選びません

この製品以外に、 30 年の研究現場への対応経験に基づいた高精度・高性能の磁気 Kerr 効果装置、Faraday 装置、 磁区観察顕微鏡など、 各種磁気光学製品の取り揃えがございます。
お気軽にお問合せください。

レーザとレーザ応用システム製品の総合メーカー
NEOARK ネオアーク株式会社
営 業 部 / 〒156-0041 東京都世田谷区大原2-17-6-108 TEL(03)6379-5539 FAX(03)6379-5688
大阪支店 / 〒541-0056 大阪市中央区久太郎町2-3-8-201 TEL(06)6271-5123 FAX(06)6271-5110
本社 第1工場・第2工場 / 八王子市
URL http://www.neoark.co.jp E-mail:info@neoark.co.jp

Journal of the Magnetics Society of Japan
Vol. 41, No. 5

Electronic Journal URL: https://www.jstage.jst.go.jp/browse/msjmag

CONTENTS

J. Magn. Soc. Jpn., **41**, 81-93 (2017)

<Review>

Basic and Applied Research of Transition-metal Based Magnetic Materials

K. Fukamichi

Professor Emeritus, Tohoku University, Sendai, Japan

Various transition-metal magnetic materials have been investigated from basic and practical viewpoints. The concentration dependence of the Néel temperature T_N of Cr-based alloys is complicated. Cr-Si and Cr-Fe antiferromagnetic alloys show Invar characteristics in the ternary alloys. Fe-based amorphous alloys exhibit weak ferromagnetic properties, resulting in remarkable magnetovolume effects. The icosahedral quasicrystals containing Mn show a spin-glass behavior, in a similar manner as those of amorphous counterparts. Itinerant-electron metamagnetic transition occurs in $La(Fe_xSi_{1-x})_{13}$, accompanied by many drastic change in magnetic and elastic properties. These drastic changes are practically useful in the field magnetic refrigeration and linear magnetostriction. The magnitude of T_N of Mn-based γ-phase is increased by addition of Ir, Ru, Rh and the spin structures change, depending on temperature and composition. Several kinds of $L1_0$-type Mn alloys have a high value of T_N with a large magnetocrystalline anisotropy. The shift of the exchange-bias field for the collinear spin structure in $L1_0$-type phase is induced by spin frustration. $L2_1$- and B2-type Co_2CrGa metallurgical stable alloys exhibit a high spin polarization. Several kinds of $L2_1$-type and B2-type alloys show a large ferromagnetic shape memory effect associated with twin-boundary motions.

Key words: antiferromagnetic Invar alloy, weak ferromagnetic Fe-based amorphous alloy, quasicrystalline alloy, spin-glass, itinerant-electron metamagnetic transition, magnetic refrigerant, giant magnetostriction, exchange- bias field, half-metalicity, ferromagnetic shape memory alloy

1. Introduction

In the present article, I introduce my several research subjects for the MSJ Award 2016. I have engaged in basic and applied research for a variety of transition-metal magnetic materials during several decades. Listed below are our main subjects: antiferromagnetism and Invar characteristics of Cr-based alloys, weak ferromagnetic Fe-based amorphous alloys, Hall resistivity of amorphous alloys, comparison between magnetic properties in quasicrystalline and amorphous states of Al-based Mn alloys, perpendicular magnetic anisotropy of Tb–Fe bulk amorphous alloys, random magnetic anisotropy and coercive field of Fe–rare earth amorphous alloys, giant magnetoresistance effect in Cu–Co granular alloys, linear magnetostriction of Fe– Pd and Fe–Ga alloys, itinerant-electron metamagnetism of Laves phase compounds and $NaZn_{13}$-type compounds exhibiting large magnetocaloric effects (MCE), spin fluctuations in β-Mn alloys, antiferromagnetism, magnetocrystalline anisotropy and exchange coupling in Mn alloys, magnetocrystalline anisotropy in Fe–Pd and Fe–Pt alloys, half-metalicity and magnetic-field induced shape memory effect in Heusler type alloys. These achievements have been contributed to publish several kinds of international monographs [1-8]. I present the results for the selected topics given in Fig. 1. The neighboring research fields in the figure share technical, magnetic and physical common terms, providing research continuity.

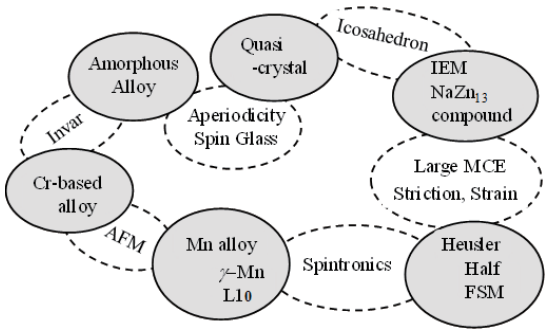

Fig.1 Correlation chart between several kinds of research topics in magnetism and magnetic materials.

2. Explanation of main topics

2.1 Antiferromagnetism and Invar characteristics of Cr-based alloys.

Cr with a bcc structure orders antiferromagnetically in a spin-density-wave (SDW) structure below T_N = 311 K, showing a prototypical itinerant antiferromagnet. It has been pointed out that pure Cr indicates a weak first-order transition at T_N. Cr-based alloys exhibit three distinct ordered phases transverse SDW (AF_1), longitudinal SDW (AF_2), and commensurate SDW (AF_0). The magnetic phase diagrams for Cr-based alloys have been studied as functions of concentration, pressure, temperature, and magnetic field [9].

We investigated magnetic properties of a number of Cr-based alloys. The transition metals at the right of Cr in the periodic table, except for ferromagnetic

elements Fe, Co and Ni, and paramagnetic Pd, increase T_N. While the transition metals at the left of Cr in the periodic table decrease T_N. For non-transition metal additions, such as Al (above 2%), Ga (above 1%), Ge, Sn, As and Sb increase T_N, although Si decreases it[10].

The wave vector, $\boldsymbol{Q}$, of the SDW is along one of the cube axes and is incommensurate with the periodicity of the lattice. The wavelength of the SDW is about 25 unit cells at room temperature and is temperature dependent. The <100> cross sections of the Fermi surface centered at Γ and H are the inter-sections of the octahedrons; the former is the electron octahedron and the latter the hole octahedron. The antiferromagnetic state is stabilized by the nesting due to the coulomb interaction between the Γ and H surfaces. When the SDW is shifted in the direction of <100>, the wave vector $\boldsymbol{Q}$ is given as

$$\boldsymbol{Q}_{\pm} = \frac{2\pi}{a}(1 \pm \delta), \tag{1}$$

where a is the lattice constant and δ is the nesting parameter[11,12]. The value of δ increases with the introduction of the transition metals at the left of Cr in the periodic table, as for V and Ti, for example. Meanwhile, δ decreases and vanishes for certain concentration of metals, as with the introduction of 3d-metal impurities like Mn, Fe, Re, changing SDW to AF_0, i.e., $\delta = 0$.

The Néel temperature T_N, which is an experimental measure of stability of the SDW, is given by an equation of the form

$$T_N = T_0 \exp\left(-\frac{1}{\lambda}\right), \tag{2}$$

where T_o is a function which depends on the band structure and

$$\lambda = \frac{\gamma^2 V(0)(k_c)^2}{2\pi^2 v}. \tag{3}$$

Here γ is the mean overlap matrix element for electrons in the same band, $V(0)$ the average screened Coulomb potential, k_c the wave vector in the first Brillouin zone and ν is the arithmetic mean of the Fermi velocities in two bands. It is considered to be senseless to predict T_N from Eq. (2) because of the exponential dependence on some of the quantities involved[11]. In such complicated circumstances, it is considered to be practically useful that Cr–Fe[13] and Cr–Si[14] alloys exhibit a strong first-order magnetic phase transition, accompanied by a large spontaneous volume magnetostriction below T_N in the AF_0 structure.

Before LCD (liquid crystal display), CRT (cathode ray tube display) had been used for long time. The CRT has an Invar alloy as a shadow mask. However, conventional Invar alloys are ferromagnetic, and then remanent magnetization and geomagnetism involve color drifts offensive to the eye. Therefore, development of non-ferromagnetic Invar alloys was a pressing issue at that time. The Invar characteristics, that is, a very low thermal expansion is associated with the cancelation of the phonon part of thermal expansion by the spontaneous volume magnetostriction. Reducing the steep volume change by addition of the third element to Cr-Fe and Cr-Si binary alloys, Invar characteristics was obtained below T_N. Practically, we require to set Invar characteristics in the vicinity of room temperature. By changing the electron concentration, the value of T_N is tunable. From these data, we can make suitable non-ferromagnetic (≡ antiferromagnetic) Invar alloys.

Figure 2 shows the thermal expansion curves of Cr–Fe–Mn alloys[15]. For comparison, we present the thermal expansion curve of a conventional Invar alloy

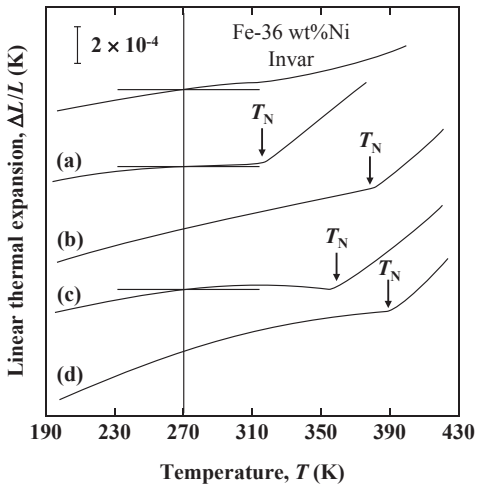

Fig. 2 Thermal expansion curves of Cr–Fe–Mn antiferromagnetic alloys, together with the curve of conventional Invar alloy (Fe–36 wt% Ni)[15].
(a) Cr-5.5%Fe-0.5%Mn, (b) Cr-25.5%Fe-1.0%Mn, (c) Cr-4.3%Fe-0.5%Mn, (d) Cr-4.2%Fe-1.0%Mn.

(Fe-36%wt%Ni). It is clear that the curves of Cr–Fe–Mn alloys exhibit an excellent Invar characteristics. On the basis of data accumulation, we developed many kinds of Cr–Fe and Cr–Si based antiferromagnetic Invar-type ternary alloys[10,16,17]. Figure 3 lists the possible combinations of elements, which are selected from the right upper grey area. In the figure, the dot-dashed line divides the border above which the Néel temperature T_N of Cr increases and below which it

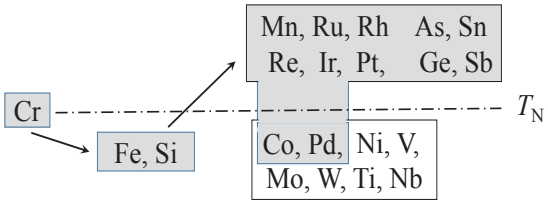

Fig.3 Combination of elements for Cr-based antiferromagnetic Invar-type ternary alloys [10,16,17].

decreases. What should be noted is that Co and Pd decrease T_N of Cr, yet increase T_N of Cr–Fe and Cr–Si alloys, exhibiting Invar characteristics around room temperature[1,10].

2.2. Weak ferromagnetic Fe-based amorphous alloys

2.2.1 Large magnetovolume and magnetoelastic properties of Fe-based amorphous alloys

Amorphous magnetic alloys provide many peculiar properties because of loss of lattice periodicity. Various amorphous alloys have been prepared by melt-quenching in a ribbon state and sputtering in a film state. Fe–metalloid systems in the equilibrium phase diagram have a relatively low eutectic point, showing an excellent forming-ability of amorphous ribbons. The striking aspect is that the number of nearest-neighbor atom in transition metal–metalloid systems is estimated to be about 13, being very close to that of the fcc lattice. Concentration dependence of the magnetic moment per Fe atom for amorphous Fe–B alloys is not monotonic and a maximum occurs around 14 at% boron[18], but then the Curie temperature T_C decreases with a decrease in the boron content. Such peculiar concentration dependences are similar to those of Fe–Ni fcc alloys which are classified as weak ferromagnets with an incomplete filling of up-spin band, resulting in Invar effects such as a low thermal expansion and a strong pressure effect on the Curie temperature T_C.

On thermal expansion curves of amorphous Fe–B and Fe–P alloys, a large anomaly due to a remarkable spontaneous volume magnetostriction is observed in a wide temperature range below the Curie temperature T_C[18]. For $Fe_{83}B_{17}$ alloy, the value of the spontaneous volume magnetostriction ω_s estimated from the thermal expansion curve is about 1×10^{-2}, being of the same of magnitude as that of crystalline Fe–Ni Invar alloys. In addition, the pressure coefficient of the Curie temperature, $\partial T_C/\partial P$, is very large negative; the largest negative value is of about –7 K/kbar, corresponding to that of $Fe_{71}Ni_{29}$ crystalline fcc alloy. According to Wohlfarth's theory on very weak itinerant ferromagnetism[19], the pressure effect on T_C is given by

$$\frac{\partial T_C}{\partial P} = -\frac{A}{T_C}, \tag{4}$$

where the parameter A is proportional to the density of states, compressibility, effective degeneracy temperature and the Bohr magneton. The data of Fe–Ni crystalline Invar alloys are in line with A = 2050 K^2/ kbar, and these of Fe–B amorphous alloys fit approximately with A = 3500 K^2/kbar. The compressibility κ calculated from the shear modulus and Young's modulus for Fe–B alloys is larger than that of Fe–Ni crystalline Invar alloys. That is, the value of the former is larger than that of the latter value by a factor of about 1.7[20]. This result is qualitatively consistent with Wohlfarth's theory because the value of A in Eq. (4) is proportional to κ.

Hitherto we have demonstrated that the magnetic properties of Fe–B amorphous Invar alloys are very similar to those of Fe–Ni crystalline Invar alloys. It has been well that Invar behavior of Fe–Ni crystalline alloys is very complicated at lower Ni concentrations because of the occurrence of a martensitic transformation. On the other hand, the magnetic properties of amorphous alloys are studied without taking such a complicated effect into consideration, because amorphous alloys involve no martensitic transformation. Accordingly, these results exclude a conventional explanation of the origin of Invar effects associated with the pre-martensitic transformation.

It is notable point that Fe–B amorphous alloys also exhibit a remarkably large ΔE effect defined as $\Delta E/E_0$ with $\Delta E = E_s - E_o$, where E_s and E_0 are Young's moduli in saturating field and in zero magnetic field, respectively. This effect is responsible for the Elinvar characteristics[21]. The temperature coefficient of the delay time t of delay lines is expressed as

$$t = -\frac{1}{2}(\alpha + e), \tag{5}$$

where α and e are the temperature coefficients of thermal expansion and Young's modulus, respectively. Fe–B amorphous alloys indicate a very small temperature coefficient of the delay time, because they have the Invar and Elinvar characteristics at the same temperature, in contrast to Fe–Ni crystalline Invar alloys which exhibit a large value of e at room temperature.

2.2.2 Forming-ability and weak ferromagnetism and spin-glass behavior of E–Fe alloy systems

There are several kinds of electron theories for forming-ability of amorphous films. According to Moruzzi et al. theory[22], a high Fermi level state density means a lack of structural stability, resulting in an amorphous state. In the case of early transition metal (E)–Fe systems, the larger the atomic size difference becomes, the higher the Fermi level becomes[23]. We systematically investigated the lower limit of solute elements vs. the size difference ratio between Fe and the solute clement. It was pointed out that the lower limit of forming-ability of amorphous films depends not only on the size difference ratio but also on the valence difference between E and Fe[3,24]. That is, the lower limit shifts to lower concentration ranges with increasing values of the size and valence differences. The energy separation in the density of state is roughly proportional to the valence difference and leads to the gradual formation of a well-defined gap for compounds [22]; namely, split-band state densities are formed by constituents with large valence differences, leading to the stabilization of an amorphous phase. Therefore, the effect of the size difference on the forming-ability is explained by the theory proposed by Moruzzi et al.

In Friedel's model[25] which is valid in the strong

ferromagnetic situation, the charge displaced by the early transition metal atom is related to the magnetization change by the simple formula $10-\Delta z$, where Δz is the host-solute valence difference. If the assumptions underlying this simple relation were obeyed over the entire concentration range, then the concentration dependence of the average moment $\bar{\mu}$ is defined as

$$\bar{\mu} = \mu_0 - x(10 - \Delta z), \tag{6}$$

where x is the atom fraction and μ_0 is the host moment at x=0. Friedel's formula Eq. (6) follows from the assumption that the repulsive solute potential displaces precisely five majority-spin states from below to above the Fermi level E_F. Implicit in the Friedel formula, therefore, is the assumption that the state density immediately above the d-bands of the paramagnetic host is negligible; this assumption is a necessary condition for strong magnetism. Figure 4 displays the concentration dependence of the mean magnetic moment $\bar{\mu}$ of E_xFe_{1-x} with E = Lu, Y, Th, Hf, Zr, Ti, Ta, Nb, V [26]. The value of $\bar{\mu}$ becomes larger as the differences of the atomic size and the valence between E and Fe increases. Such a systematic tendency is explained from the band calculation[23]. In the figure, three dotted straight lines indicate the expected line from Friedel's model which is valid for strong ferromagnets. Since the observed values are smaller than the expected values of dotted straight lines, E_xFe_{1-x} amorphous systems are regarded as weak ferromagnets which have holes in both d-bands.

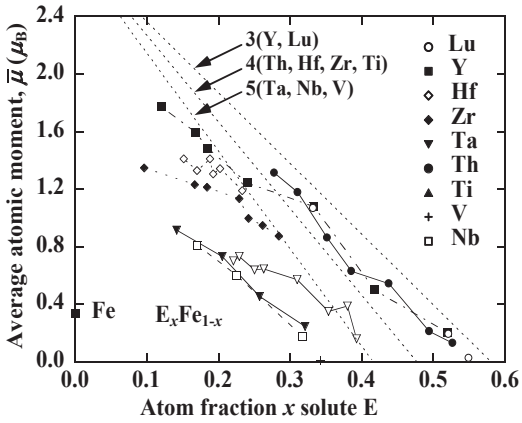

Fig.4 Average low temperature magnetic moment $\bar{\mu}$ of amorphous Fe alloys with many kinds of early transition metal solutes (E) as a function of atomic fraction x[26].

The Curie temperature T_C of E_xFe_{1-x} amorphous films with E=La, Lu, Ce, Hf and Zr exhibits a broad maximum at x=0.2 and the ferromagnetic state diapers around x=0.1, resulting in a spin-glass state below about 110 K[3,27]. This spin-glass state is caused by spin frustrations in the magnetically concentrated E_xFe_{1-x} amorphous alloys. It is meaningful to note that the nearest neighbor distance of Fe, $d_{Fe\text{-}Fe}$, is about 2.5 Å[28], very close to the critical distance of ferromagnetic and antiferromagnetic interactions.

2.3 Comparison between magnetic properties in quasicrystalline and amorphous states of Al-based Mn alloys

Electron diffraction studies revealed that Al–Mn quenched alloys exhibit sharp spots with five-fold symmetry axes[29]. This discovery contradicts a well-known crystallographic theorem which states that five-fold symmetry axes can never appear in substances having a truly long-range periodicity. A quasiperiodic crystal, or quasicrystal, is a structure that is ordered but not periodic. A quasicrystalline pattern can continuously fill all available space, but it lacks translational symmetry. While crystals, according to the classical crystallographic restriction theorem, can possess only two, three, four, and six-fold rotational symmetries, the Bragg diffraction pattern of quasicrystals shows sharp peaks with other symmetry orders, for instance five-fold.

It has been pointed out that computer simulations of the supercooled Lennard Jones pair potential suggest the existence of bond orientation order in liquids [30]. Because icosahedral clusters which are composed of 13 atoms have a significantly lower energy compared with that of nuclei of fcc and hcp crystals, icosahedra should be prevalent in liquids near the melting temperature [31,32]. It has been remarked that an amorphous Lennard-Jones packing has about 32% of its atoms on icosahedral sites[33], and the scattering patterns observed in several amorphous alloys are quite similar to those from icosahedral clusters. The sign of the exchange interaction oscillates between positive and negative depending on the Mn–Mn distance. It is therefore interesting to study the magnetic properties of quasicrystalline and amorphous alloys containing Mn.

We investigated magnetic properties of Al–Cu–TM and Al–Pd–TM (TM: transition metal) quasicrystalline alloys[4,34]. The difference between the quasicrystalline alloys and their amorphous counterparts for magnetic properties was confirmed in Al–Cu–Mn and Al–Pd–Mn alloy systems in contrast to Al–Mn alloy system.

The magnetization is much smaller than the value expected from the effective magnetic moment P_{eff} (μ_B), indicating that the magnitude of magnetic moment is not uniform, depending on the Mn sites in the quasicrystalline phase. From many kinds of experiments, it was confirmed that there are magnetic and non-magnetic Mn atoms. The Curie constant C is written as

$$C = \frac{N\mu_B{}^2 < P_c > (< P_c > +2)}{3k_B}, \tag{7}$$

where N is the atomic number[35]. The average local

Table 1 The ratio of magnetic Mn atoms, X_m/X, the effective magnetic moment P_{eff}, the spin freezing temperature T_f for $Al_{85}Mn_{15}$, $Al_{65}Cu_{20}Mn_{15}$ and $Al_{65}Pd_{20}Mn_{15}$ alloys in icosahedral quasicrystalline (Q) and amorphous (A) states[34,36].

Alloy	X_m/X (%)	P_{eff} (μ_B)	T_f (K)
Q-$Al_{85}Mn_{15}$	~9*	0.59	–
A-$Al_{85}Mn_{15}$	~9*	0.59	–
Q-$Al_{65}Cu_{20}Mn_{15}$	8.9	1.56	6.1
A- $Al_{65}Cu_{20}Mn_{15}$	18.7	2.24	8.1
Q-$Al_{65}Pd_{20}Mn_{15}$	9.3	2.25	10.0
A- $Al_{65}Pd_{20}Mn_{15}$	18.7	2.54	13.9

*: extrapolated from the high Mn concentration range

magnetic moment per Mn atom, $<P_c>$, which corresponds to the saturation magnetization is deduced from the Curie constant by assuming g factor to be 2. Using the values of the Curie constant, C, and the saturation magnetization per Mn atom, M_s, one can evaluate the atomic fraction, X_m from the following relations[35]:

$$M_s\left(\frac{X}{X_m}M_s + 2\mu_B\right) = \frac{3k_BC}{N}. \quad (8)$$

Comparing with the same magnitude of P_{eff} (μ_B), the composition of Mn for Al–Mn is much higher than that for the other two alloy systems, suggesting that the formation of the localized magnetic moment in Al–Mn is much difficult than in the latter systems. The value of P_{eff} (μ_B) of Al–Mn in the amorphous (A) and quasicrystalline (Q) states is the same each other. However, the difference between the amorphous (A) and quasicrystalline (Q) states for Al–Cu–Mn and Al–Pd–Mn alloy systems is distinct as seen from Table 1[34]. Note that the latter two alloy systems contain Cu or Pd in which the localized magnetic moment is easily established. In Table 1, the ratios of magnetic Mn atoms X_m/X in Al–Cu–Mn and Al–Pd–Mn quasicrystalline alloys are about one half that of the amorphous counterparts, although there is no essential distinction in Al–Mn alloy systems[34,36]. The spin-glass behavior has been confirmed in both Al–Cu–Mn and Al–Pd–Mn alloy systems even below 15 %Mn, although Al–Mn alloys exhibit the spin-glass behavior above 20 %Mn. In addition, it is a noteworthy fact that $Al_{70}Pd_{15}Mn_{15}$ quasicrystalline alloy has a giant magnetic moment in a similar manner as Pd–Mn crystalline dilute alloys. The difference between the A- and Q-state of the spin-glass freezing temperature T_f, and the ratio of magnetic Mn atom as well, arises from the looser packing structure of the A-state, resulting in a larger Mn–Mn distance.

2.4 Itinerant-electron metamagnetism of $NaZn_{13}$-type compounds

2.4.1 Giant magnetocaloric and magnetostriction of $La(Fe_xSi_{1-x})_{13}$ system

The itinerant-electron metamagnetic (IEM) transition is the field-induced first-order transition from the paramagnetic (PM) to the ferromagnetic (FM) state in the itinerant-electron system. Wohlfarth and Rhodes[37] first discussed it on a phenomenological Landau theory. The relation between the magnetic free energy $F(M)$ and the magnetization M is given as

$$F(M) = \frac{1}{2}aM^2 + \frac{1}{4}bM^4 + \frac{1}{6}cM^6, \quad (9)$$

where the Landau expansion coefficients a, b and c are related to the 3d-electron band structures at the Fermi level E_F. The conditions of $a > 0$, $b < 0$, and $c > 0$ with $3/16 < ac/b^2 < 9/20$ are essential for the metamagnetic transition. The IEM transition is related to the onset of the exchange splitting in the band structure by applying magnetic field. This metamagnetic transition is termed 'Itinerant-electron metamagnetism (IEM)', different from a conventional metamagnetism in the localized electron system, where the metamagnetic transition (MT) takes place from the AFM to the FM state. We experimentally confirmed for the first time by using pulsed ultra-high magnetic fields that the values of the critical field for the metamagnetic transition of exchange-enhanced para-magnets YCo_2 and $LuCo_2$ Laves phase compounds are 69 and 71 T, respectively[38]. These values are relatively smaller than the theoretical values, which is reasonably explained by taking into magnetovolume effect. Furthermore, the IEM transition phase diagrams of quasi-binary systems of $Y(Co_{1-x}M_x)_2$ and $Lu(Co_{1-x}M_x)_2$ (M: Al, Ga, Si)[39] are consistent with the theoretical phase diagram obtained by taking into the effect of spin fluctuations[40].

$La(Fe_xAl_{1-x})_{13}$ compounds crystallize in the cubic $NaZn_{13}$-type structure composed of icosahedral clusters referred in Section 2.3 with two crystallographic sites: 8b and 96i. The 8b site at the center of the icosahedral cluster is occupied by Fe^I atom only. The 96i sites at the apex of the icosahedron are randomly occupied by Fe^{II} atoms and Al atoms[41]. In these compounds, the high coordination numbers of Fe atoms and the shortest Fe–Fe interatomic distance of $d_{Fe\text{-}Fe}$ ≈2.5Å are realized. Such a densely packed structure with Fe atoms results in a variety of magnetic states with a different volume related to the itinerancy of Fe3d-electron[42]. Note that the icosahedra exist even in $La(Fe_xAl_{1-x})_{13}$ in the amorphous state[5]. Furthermore, we demonstrated that $La(Fe_xSi_{1-x})_{13}$ compounds exhibit the IEM transition[43]. The IEM transition is accompanied by drastic changes in magnetic and elastic properties due to the first-order phase transition. These changes are very attractive from the practical point of view. The cubic $NaZn_{13}$-type

$La(Fe_xSi_{1-x})_{13}$ compounds (space group $Fm\bar{3}c$) have a ferromagnetic ground state. In the concentration $0.86 \leq x \leq 0.90$, the field-induced first-order magnetic transition between the ferromagnetic (FM) and paramagnetic (PM) states, that is, the itinerant-electron metamagnetic (IEM) transition, takes places above the Curie temperature T_C. We have pointed out that this IEM transition causes a large isothermal magnetic entropy change ΔS_m and a large adiabatic temperature change ΔT_{ad}[44].

In principle, the magnetic cooling system is equivalent to conventional gas cooling systems. That is, thermodynamic parameters V (volume) corresponds to $-M$ (magnetization) and P (pressure) is changed by H (magnetic field). Therefore, the Maxwell relation is given by the following expression:

$$\left(\frac{\partial S}{\partial H}\right)_T = \left(\frac{\partial M}{\partial T}\right)_H, \tag{10}$$

and hence the isothermal magnetic entropy change ΔS_m is expressed as

$$\Delta S_m = \int_0^H \left(\frac{\partial M}{\partial T}\right)_H dH. \tag{11}$$

From Eq. (11), it is expected that the magnitude of ΔS_m becomes very large when the magnetic transition is of first-order. Be aware that the magnetization change at the first-order transition is ideally discontinuous, and then the value of $\partial M/\partial T$ does not exist. Under such a condition, ΔS_m should be calculated by the Clausius–Clapeyron equation given by the following equation:

$$\left|\frac{\Delta T}{\Delta H_c}\right| = \left|\frac{\Delta M}{\Delta S}\right|, \tag{12}$$

where ΔM is the difference between magnetization before and after the discontinuity for a given T, ΔH_C is the shift of critical field from ΔT and ΔS is the difference between the entropies of the two phases. In experiments, however, a complete discontinuous magnetization data at the first-order transition temperature is scarcely obtained due to frozen disorders[45]. Figure 5 illustrates the temperature dependence of ΔS_m in the magnetic field change from 0 to 5 T ($\mu_0 \Delta H$ =5 T) obtained by using Eq. (11) for $La(Fe_{0.88}Si_{0.12})_{13}$ compound[44]. The value of $\partial M/T$ exhibits a large value around T_C because of the thermal-induced first-order transition, and T_C is increased by the magnetic field, keeping a large value of $\partial M/T$. Consequently, ΔS_m in $\mu_0 \Delta H$ =5 T indicates a negative maximum value of 22.3 J/kgK at T_C =195 K. Note that the magnitude of ΔS_m obtained from Eq.(11) is comparable with that calculated from Eq. (12). The adiabatic temperature change ΔT_{ad} is obtained from

$$\Delta T_{ad} = -\int_0^H \frac{T}{C_H}\left(\frac{\partial M}{\partial T}\right)_H dH = [T(S)_H - T(S)_0]_S \cong \frac{T}{C_t}\Delta S_m, \tag{13}$$

where $C_H = T(\partial S/\partial T)_H$ and C_t are the heat capacity in the magnetic field and the total heat capacity, respectively. Figure 6 shows the temperature dependence of ΔT_{ad} in $\mu_0 \Delta H$ =1–5 T for $La(Fe_{0.88}Si_{0.12})_{13}$ compound[44]. The value of ΔT_{ad} exhibits a large peak above T_C and the maximum value of ΔT_{ad} is 8.6 K in $\mu_0 \Delta H$=5 T at 195 K.

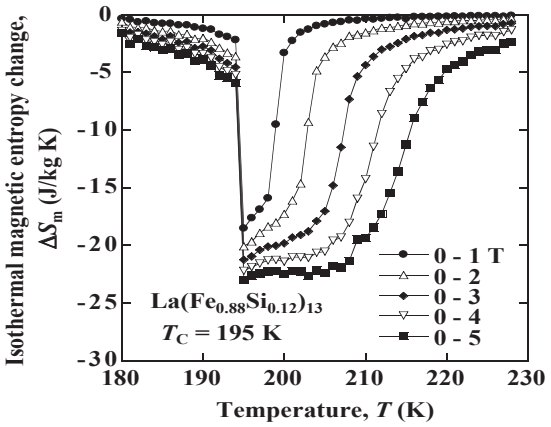

Fig. 5 Temperature dependence of the isothermal magnetic entropy change ΔS_m for $La(Fe_{0.88}Si_{0.12})_{13}$ compound[44].

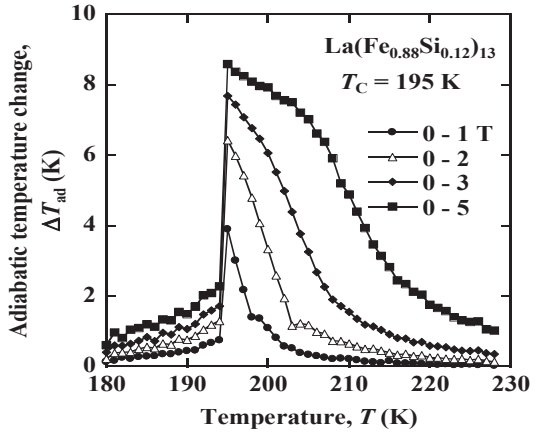

Fig. 6 Temperature dependence of the adiabatic temperature change ΔT_{ad} for $La(Fe_{0.88}Si_{0.12})_{13}$ compound[44].

The value of T_C of $La(Fe_xSi_{1-x})_{13}$ compounds is increased significantly by hydrogen absorption, accompanied by a marked volume expansion[44]. The cubic $NaZn_{13}$-type structure is kept after hydrogen absorption. Furthermore, the thermomagnetization curves still exhibit a significant magnetization change around T_C, because the thermal-induced first-order transition is maintained after hydrogen absorption[44]. The magnitude of $\partial M/\partial T$ around T_C=323 K for the compound with hydrogen concentration y =1.5 is almost the same as that of the compound with y =0.0 and T_C=195 K. After annealing at about 400 K, T_C is hardly changed, and hence the desorption of the hydrogen for $La(Fe_{0.88}Si_{0.12})_{13}H_y$ compounds scarcely proceeds below 400 K, because T_C is significantly sensitive to y.

Furthermore, tuning T_C by adjusting constituent elements, we can set up magnetic refrigerator systems in a wide working temperature range from 60 to 340 K[46]. From these data, it is concluded that $La(Fe_xSi_{1-x})_{13}$ and their modified compounds are promising magnetic refrigerants.

2.4.2 Isotropic volume magnetostriction

It has been pointed out theoretically that the onset of the magnetic moment accompanied by the IEM transition results in a volume change due to the magnetovolume effect. For x=0.88, the magnetic moment caused by the IEM transition exceeds 1 μ_B and results in a huge positive volume magnetostriction of about 1.5% just above T_C[47]. The volume magnetostriction ω_s of the IEM transition is due to the onset of magnetic moment caused by exchange splitting of 3d-electron bands and given as[48]

$$\omega_s(T) = \kappa C_{mv}\{M(T)^2 + \xi_p(T)^2\}, \quad (14)$$

where κ is the compressibility and C_{mv} is the magnetovolume coupling constant. The mean square amplitude of spin fluctuation is given by $\xi_p(T)^2$. The origin of the huge magnetostriction in $La(Fe_xSi_{1-x})_{13}$ compounds is correlated with electronic state of 3d-electrons of Fe, different from the single-ion magnetoelastic coupling in $TbFe_2$-based magnetostrictive materials. Therefore, it is expected that $La(Fe_xSi_{1-x})_{13}$ compounds are candidates as new-type high performance magnetostrictive materials. It is notable that the transition field of the IEM transition at T_C equals zero and increases with temperature.

The maximum value of thermal expansivity, $\Delta L/L$, of $La(Fe_{0.88}Si_{0.12})_{13}$ compound greatly exceeds the value of $\Delta L/L$ of the polycrystalline $TbFe_2$ compound. As is well known, $TbFe_2$-based magnetostrictive materials exhibit a large $\lambda_{//}-\lambda_{\perp}$, while the volume change $\lambda_{//}+2\lambda_{\perp}$ is nearly zero and the magnetostrictive properties are anisotropic. These anisotropic magnetostrictive properties of $TbFe_2$ compound are mainly originated from the rotation of the localized magnetic moment of Tb. The polarization of 3d-electron bands causes a volume change proportional to the square of the local magnetization as given Eq. (14) and not only $\lambda_{//}-\lambda_{\perp}$ but also $\lambda_{//}+2\lambda_{\perp}$ has finite values. A spontaneous volume change of 1.2 % occurs sharply at T_C and the value of three times of $\Delta L/L$ is very close to that of the volume change at T_C. Therefore, these results indicate that the volume magnetostriction is due to the transition from the PM phase with a small volume to the FM phase with a large volume and its volume change is almost isotropic[47]. Such isotropic magnetostrictive properties are very attractive compared to those of $TbFe_2$-based anisotropic magnetostrictive materials, because a huge magnetostriction can be obtained even in a poly-crystalline state. Accordingly, no crystallographic texture control such as directional solidification is essential. It is necessary to adjust the Curie temperature in order to obtain a huge magnetostriction in low fields around room temperature. It is notable that an isotropic giant linear magnetostriction due to the IEM transition for $La(Fe_xSi_{1-x})_{13}H_y$ compounds is also observed in the vicinity of room temperature [49].

2.5 Antiferromagnetism, magnetocrystalline anisotropy and exchange coupling in Mn alloys

2.5.1 Mn rich disordered (γ-Mn) and ordered $L1_2$ alloys

Practically, the giant magnetoresistance (GMR) and tunnel magnetoresistance (TMR) are very important for electronic and magnetic devices such as magnetic recording heads and magnetic random access memory (MRAM) cells. There are many systems having a complex (non-collinear) spin structure, depending on the d-electron number and the crystal structure associated with the geometrical frustration of magnetic moments. Exchange-biasing characteristics and the blocking temperature are closely correlated with the spin structures and the magnitude of the Néel temperature T_N.

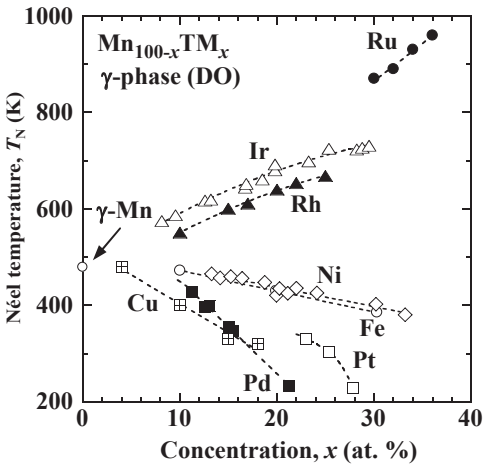

Fig. 7 Concentration dependence of the Néel temperature, T_N, for the disordered γ (fcc)-phase $Mn_{100-x}TM_x$ alloys (TM=Ir, Ru, Rh, Ni, Fe, Pt, Pd and Cu)[7,8,50].

The γ (fcc)-phase disordered (DO) Mn-based alloys are stabilized by several kinds of additional elements in analogy with Fe-based γ-phase alloys. The concentration dependence of T_N of $Mn_{100-x}TM_x$ γ-phase disordered alloy systems (TM: Transition Metal) is gathered in Fig. 7[7,8,50]. The value of γ-Mn pure metal is added in the same figure, for comparison. The lower the electron concentration, and also the larger the atomic size of additive elements such as Ru, Rh and Ir, the higher the Néel temperature T_N becomes. What has to be noticed is that the magnitude of for the disordered γ-phase Mn–Rh and Mn–Ir alloys is lower by 150–200 K than that for ordered $L1_2$-type (≡ Cu_3Au-type) counterparts, depending on the alloying element and its composition.

In the 1Q and 2Q SDW structures in γ (fcc)-phase disordered Mn-based alloys, the magnetic moment points to the parallel and the perpendicular to the *c*-axis, respectively. Take heed that the angles θ and ϕ are defined individually for each site. When ϕ is settled at 45 degrees, θ=0, θ= 90 and $\theta = \cos^{-1}(1/\sqrt{3}) = 54.7$ degrees correspond to the so-called 1Q, 2Q and 3Q SDW structures (see the top panel of Fig. 9), respectively, which are labeled multiple-Q SDW structures. In the γ-phase disordered Mn alloys, the 1Q, 2Q and 3Q SDW structures are observed by changing temperature and/or composition[7,8,50].

2.5.2 $L1_0$-type Mn alloys and exchange coupling

In the vicinity of the equiatomic concentration, Mn forms alloys with Ni, Pd, Pt, Rh and Ir in a wide range of concentration. The crystal structure of these alloys is a B2 (CsCl)-type cubic phase at high temperatures and transforms into an $L1_0$ (CuAu-1)-type tetragonal phase with a diffusionless martensitic transformation process at low temperatures[8,50]. The $L1_0$-type phase has a collinear antiferromagnetic structure (AF-1) and MnNi, MnPd and MnPt equiatomic alloys indicate a very high Néel temperature T_N of about 1100, 780 and 970 K, respectively[8,50]. Due to such a high stability of antiferromagnetism, especially, MnPt alloy has been investigated intensively from the viewpoint of practical applications as antiferromagnetic pinning layers of GMR and TMR devices. Moreover, the linearized muffin-tin orbitals (LMTO) band calculations including the spin-orbit interaction were performed for MnPt in order to investigate the magnetocrystalline anisotropy energy (MAE) because it plays an important role in the exchange-bias field in spin valves. By using the force theorem, the MAE is obtained from the following expression:

$$\Delta E_{MAE} = E[100] - E[001], \tag{15}$$

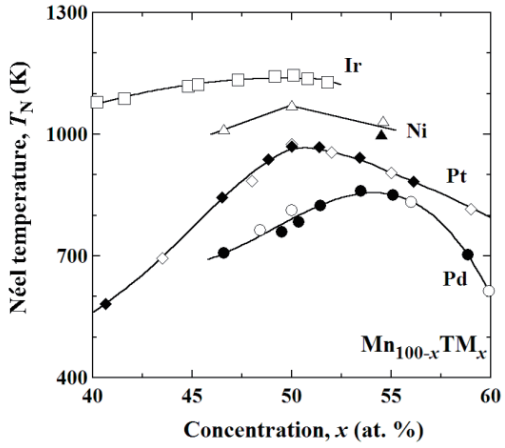

Fig. 8 Concentration dependence of the Néel temperature, T_N, for the $L1_0$-type $Mn_{100-x}TM_x$ alloys (TM: Ir, Ni, Pt and Pd))[7,8,50].

where E [n] is the sum of the eigenvalues of the Kohn–Sham equation[52] when the magnetic moment is parallel to the crystal axis [n] in the $L1_0$-type structure. The magnetocrystalline anisotropy constant of MnPt equiatomic alloy is calculated to be about 1.39 x10^6 Jm^{-3}, larger in magnitude with the positive sign larger than that with the negative sign of MnNi equiatomic alloy[51]. Plotted in Fig, 8 is the concentration dependence of T_N of $L1_0$-type ordered MnIr, MnNi, MnPt and MnPd alloys[8,50]. The MnIr alloy system exhibits the highest value of T_N in the whole concentration range. In addition, attention should be paid to that the concentration dependence of T_N for this alloy system is not so sensitive, compared with that of the others of $L1_2$-type ordered alloy systems.

The relationship between the spin structure and the magnetization loop is provided in Fig, 9[53]. The top panel represents the magnetic primitive cells constituted of four atoms in the γ (fcc)-phase structure. The presence of non-magnetic atoms changes the number of interacting spins at the nearest neighboring atomic sites, causing the spin frustration in the γ-phase disordered alloy system. This spin frustration lowers the energy of the 3Q spin structure, compared with that of the collinear spin structure[54]. The initial spin configuration is assumed to be in the 1Q structure, and hence the final solution is obtained to be the 3Q spin structure in the case of the disordered alloy with 75% magnetic atoms and 25% non-magnetic atoms. The spin configuration of the ordered AFM layer having the $L1_0$-type lattice structure was also calculated by using the Monte Carlo method. Two magnetic and two non-magnetic atoms are included in the magnetic unit cell. The spin correlation angle between the nearest neighboring spins indicates 180 degrees and it corresponds to the AF-1 spin structure, being a typical collinear spin structure of AFM alloys.

The magnetization process in an external field was calculated by adding the FM layer to such AFM layers. The motion equation of spins was solved directly within the framework of the classical Heisenberg model[53].

$$\mathcal{H} = -\sum_{(i,j)} J_{1ij}(\boldsymbol{S}_i \cdot \boldsymbol{S}_j) - \sum_{(i,k)} J_{2ik}(\boldsymbol{S}_i \cdot \boldsymbol{S}_k) - \sum_i D_i (\boldsymbol{S}_i \cdot \boldsymbol{n}_i)^2 - g\mu_B \sum_i (\boldsymbol{S}_i \cdot \boldsymbol{H}_{app}), \tag{16}$$

where the unit vector S_i denotes the spin at the ith atom, and the summation is made over all possible spin pairs by using the exchange constants, J_1 and J_2. The indices j and k respectively represent the first and second nearest neighboring spins for ith atom. The summations for j and k are firstly carried out with fixed i, and later on, the summation for i is carried out on all atoms. The spin pairs <i, j> and <i, k> represent the summations by such the procedure. The third and fourth terms in Eq. (1) describe the magnetic anisotropy energy and the Zeeman energy, respectively. The g-factor is given by g, D_i, and the unit vector $\boldsymbol{n}_i$, respectively stand for the anisotropy applied field is

given by $\boldsymbol{H}_{app}$. The magnetic easy axis $\boldsymbol{n}$ and the applied field $\boldsymbol{H}_{app}$ point to the [011] and the [2$\bar{1}\bar{1}$] directions, respectively. As seen from the figure, the AFM/FM bilayer with the 1Q, 2Q or AF-1 structures only displays the coercivity in the magnetization loop without any shift. That is, only the 3Q structure can realize the loop shift caused by the unidirectional exchange-bias field[53]. At first glance, the above-mentioned model seems to be invalid for the formation of unidirectional exchange-bias field in the collinear systems. As a solution to explain existing experimental data, we need to introduce the frustrated spins due to the interfacial roughness and defects into the ordered $L1_0$-type AFM layer. In consequence, the calculated magnetization loop is actually shifted by the unidirectional exchange-bias field even in the ordered $L1_0$-type alloys.

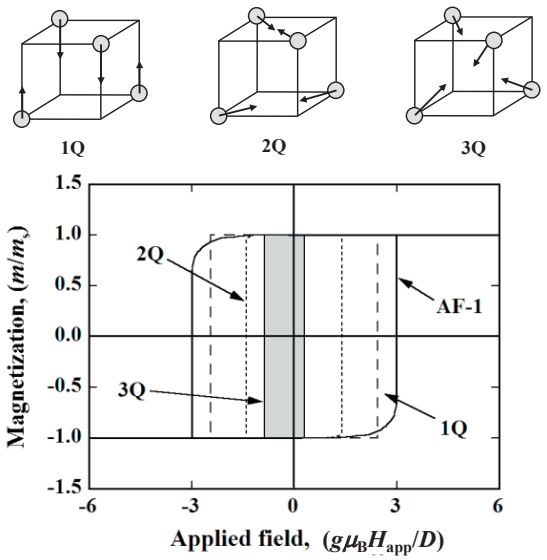

Fig. 9 Spin structures in the magnetic primitive cell of the γ (fcc)-phase lattice and magnetization loops of the AFM/FM bilayer for 1Q, 2Q, 3Q and AF-1 spin structures[53].

2.6 Half-metalicity and field induced shape memory effect in Heusler alloys

2.6.1 Half metal Heusler alloys

The magnetic tunnel junctions (MTJs) are required for spintronic devices such as magnetic random access memories and magnetic sensors. Half-metallic ferromagnets (HMFs) with a high spin polarization ratio P have intensively been investigated as spintronic devices because MTJs using the HMFs are expected to exhibit a large value of TMR as given by the following expression:

$$TMR = \frac{2P_1P_2}{1-P_1P_2}, \tag{17}$$

where P_1 and P_2 are the spin polarization ratio of electrodes[55]. The spin polarization ratio P is obtained from the following expression[56]:

$$P(\%) = \left|\frac{N_\uparrow(E_F) - N_\downarrow(E_F)}{N_\uparrow(E_F) + N_\downarrow(E_F)}\right| \text{x}100, \tag{18}$$

where $N_\uparrow(E_F)$ and $N_\downarrow(E_F)$ denote the density of states (DOS) at the Fermi level E_F in the majority and the minority spin states, respectively. In the band structure of half-metallic compounds the minority band is semiconducting with a gap at E_F, leading to 100% spin polarization at E_F.

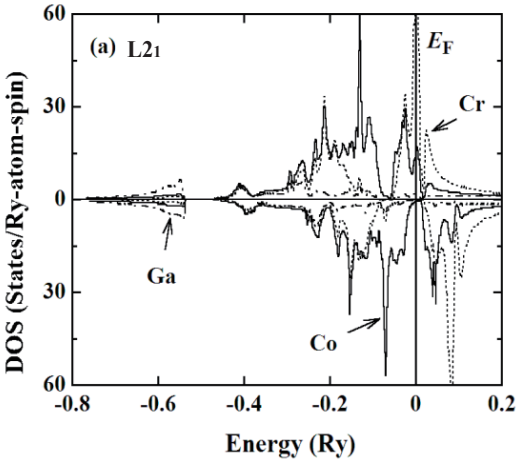

Fig. 10 Density of states of the Co_2CrGa alloy with the $L2_1$-type structure. The upper and lower curves in each panel correspond to the majority and the minority spin states, respectively[57].

The DOS calculated by the LMTO method in the atomic sphere approximation (ASA) for the $L2_1$ and B2-type (= high temperature phase of $L2_1$) structures of Co_2CrGa alloy are sketched in Figs. 10 and 11, respectively[57]. For the calculations of B2-type structure, the coherent potential approximation (CPA) method was cooperated. The upper and lower curves in each figure refer to the majority and minority spin states, respectively. The DOS of the $L2_1$-type structure in Fig. 10 exhibits a half-metal-type electronic structure. As shown in Fig. 11, the DOS of B2-type is almost half-metal type and exhibits a high spin polarization. By using J_0 regarded as the effective exchange constant, T_C^{cal} is calculated from the following equation within the mean-field approximation for spin systems[57].

$$T_C^{cal} = \frac{2J_0}{3k_B}, \tag{19}$$

where k_B is the Boltzmann constant.

The calculated magnetic moment of each atom M^{cal} (μ_B/atom), the calculated total magnetic moment M_{tot}^{cal} (μ_B/f.u.), the calculated spin polarization P (%), the

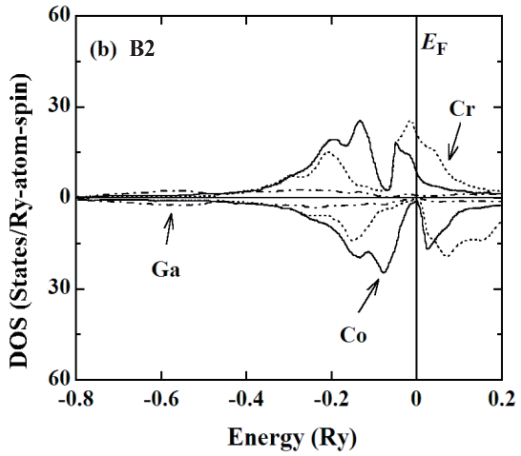

Fig. 11 Density of states of the Co_2CrGa alloy with the B2-type structure. The upper and lower curves in each panel correspond to the majority and the minority spin states, respectively[57].

saturation magnetic moment at 4.2 K M_s (μ_B/f.u.), the experimental Curie temperature T_C^{exp} (K), and the calculated Curie temperature T_C^{cal}(K) obtained in the molecular field approximation scheme for Co_2CrGa alloys with the $L2_1$ and B2-type structures are listed in Table 2 [57]. The saturation magnetic moment M_s at 4.2 K is 3.01μ_B/ f.u., being consistent to the theoretical value and the generalized Slater-Pauling line given by

$$M_t = Z_t - 24, \tag{20}$$

where M_t and Z_t are, respectively, the total values of magnetic moment and valence electron numbers in the unit cell. Furthermore, it is clear from the theoretical calculations that the band structure of B2-type structure also exhibits a half-metal type and the calculated Curie temperature T_C is about 100 K lower than that of the $L2_1$-type structure. Metallurgically, it is noteworthy to note that the $L2_1$-type phase of Co_2CrGa is much more stable, compared with that of $Co_2Cr_{1-x}Fe_xAl$[58]. In $Co_2Cr_{1-x}Fe_xAl$ alloy system, the systematic theoretical calculations have been carried out, and pointed out that the disordering between the Al and the (Cr, Fe) sites scarcely degrades the spin polarization[58]. Conversely, the disordering between the Co and the (Cr, Fe) sites brings about a significant reduction of the spin polarization[58]. In fact, a spinodal decomposition inevitably takes places in Co_2CrAl alloy, resulting in reductions of the saturation magnetic moment and the Curie temperature[59].

Table 2 The calculated magnetic moment of each atom M^{cal} (μ_B/atom), the total magnetic moment M_{tot}^{cal} (μ_B/f.u.), the spin polarization P (%), the saturation magnetic moment M_s (μ_B/f.u.) at 4.2 K, calculated and experimental Curie temperatures T_C^{cal} and T_C^{exp}(K) of Co_2CrGa alloys for the $L2_1$ and B2-type structures[57].

Structure	M_{Co}^{cal} (μ_B/atom)	M_{Cr}^{cal} (μ_B/atom)	M_{Gd}^{cal} (μ_B/atom)	M_{tot}^{cal} (μ_B/f.u.)	M_s^{exp} (μ_B/f.u.)	P (%)	T_C^{cal} (K)	T_C^{exp} (K)
$L2_1$	0.90	1.28	- 0.07	3.01	3.01	95	419	495
B2	0.82	1.44	- 0.06	3.03	–	84	295	–

2.6.2 Ferromagnetic shape memory alloys

Field-induced strains in ferromagnetic shape memory alloys (FSMAs) attract a great deal of attention as smart materials. Because FSMAs exhibit both a reversible martensitic transformation and ferromagnetism, one can control the shape memory effect by applying magnetic field in addition to conventional controls by temperature and stress. Field-induced strain in ferromagnetic shape memory alloys is due to twin-boundary motion and the strain is tied to the crystallography, not the direction of magnetization. That is, it is possible to rotate the direction of magnetization with no FSMA strain, only conventional magnetostriction, in FSMAs of relatively weak anisotropy. In magnetostrictive materials, on the other hand, field-induced strain is a result of magnetization rotation relative to the crystallography; the strain is tied to the direction of magnetization, not the lattice.

In the martensite phase of FSMAs, the giant magnetic-field-induced strains (MFIS) have been observed in Ni_2MnGa Heusler alloy[60]. This phenomenon is concerned with the rearrangement of twin variants. The MFIS depend on the crystallographic orientation, because twin-boundary motions are closely related with both the magnetocrystalline anisotropy and the Zeeman energies[60,61]. The martensitic transformation takes place from a $L2_1$ (cubic) parent phase to a $D0_{22}$ (tetragonal) martensite phase. When the martensitic transformation occurs, some variants are introduced in consequence of the minimum elastic energy. Furthermore, microscopic magnetic domains exist in martensite twin variants so as to reduce the magnetic dipole energy. The magnetic domains not

parallel to the direction of applied magnetic field H are diminished on applying H, and then magnetization M changes direction to the magnetic field direction. The twin variants rearrange and twin boundary is moved in connection with the rotational magnetization, accompanied by macroscopic strains, when the magnetocrystalline anisotropy energy is larger than the driving energy to rearrange the twin variants.

In order to satisfy the condition for the variant rearrangement by applying magnetic field, the magnetic shear stress τ_{mag} should be larger than the mechanical shear stress τ_{req} required for the variant rearrangement. Stated differently, the following criterion should be satisfied

$$\frac{|K_u|}{s} = \tau_{mag} > \tau_{req}, \tag{21}$$

where K_u is the magnetic anisotropy constant[62]. The value of τ_{mag} is expressed as $|K_u|/s$, s is the corresponding twinning shear calculated by using the lattice parameter ratio c/a of the $L1_0$-type martensite phase. The twinning plane is $\{101\}_P$ for Co–Ni–Ga system, therefore the twinning shear s is expressed as

$$s = \frac{\{1-(c/a)^2\}}{(c/a)}. \tag{22}$$

When the magnitude of shear stress becomes $\tau_{mag} < \tau_{req}$, the condition given by Eq. (21) is not satisfied. As a result, one can obtain no MFIS. In other words, a high twinning stress is required to induce the twinning transformation in the $L1_0$ structure. Therefore, we need a static applied twinning stress σ_{tw} to assist τ_{mag}. We have developed a new group of FSMAs in the Co–Ni–Al B2-based alloy system[63,64], which is characterized by good ductility and a wide range of transition temperatures. Because the composition range of these FSMAs is located near the B2+γ two-phase region, these alloys are amenable to the introduction of the γ-phase by proper choice of composition and heat treatment temperature. The hot-workability and room temperature ductility of these alloys are significantly improved by the introduction of the γ-phase, which is a good advantage for practical applications[62]. The structure of parent phases, the lattice constant ratio c/a of martensite phases and the value of strain of the FSMs mentioned above are summarized in Table 3.

Table 3 The crystalline structure, the lattice constant ratio c/a, the value of strain of several kinds of $L2_1$- and B2-type ferromagnetic shape memory alloys[62,65-67].

Alloy	Structure	c/a	Strain (%)	Remark	Reference
$Ni_{49}Fe_{18}Ga_{27}Co_6$	$L2_1$	1.20	-8.5	SA	65
$Ni_{49.5}Fe_{14.5}Mn_{4.0}Ga_{26.0}Co_{6.0}$	$L2_1$		-11.3	SA	66
$Co_{47.5}Ni_{22.5}Ga_{30.0}$	B2	1.18	-7.6	SA	67
$Co_{41}Ni_{32}Al_{27}$	B2+γ	1.16	-3.3	SA, ductile,	62

SA: stress assisted

3. Closing remarks

Important recent progress has been made in the theoretical and experimental fields given in Fig.1. It has been pointed out that the nesting of Fermi surfaces for electron-hole pairs in Cr is associated with the superconductivity for electron-electron pairs, and mathematically the nesting model is identical to the BCS model for superconductivity. The coexistence of SDW and superconductivity in various compound systems have been reported. Therefore, the discussion on the relation between SDW and superconductivity would become active[68]. The concentration dependence of Cr-based alloys is in diverse ways, depending on additives. The formation of local moments such as Fe, Co, or Ni, might strongly modify the behavior of Cr and decreases T_N[9]. However, strange that Cr-Fe-Co ternary alloys increase T_N as discussed in connection with Fig. 3.

Since the discovery of giant magnetoresistance in multilayers of Fe/Cr, great effort has been done in understanding the magnetic coupling through chromium antiferromagnetic layers[69]. Many data are very intricate because the SDW state depends on many factors such as temperature, film thickness, interface exchange coupling, hybridization with the adjacent layers and interface roughness.

A finite-temperature theory of magnetism that takes into account the fluctuations of local magnetic moments due to structural disorder has been discussed on the basis of the functional-integral method with the method of the distribution function[70]. The results of numerical calculations point that amorphous iron forms an itinerant-electron spin-glass at low temperatures because of the nonlinear magnetic coupling between Fe local moments and the local environment effect on the amplitude of the Fe local moment due to the structural disorder. It should be emphasized that the calculated spin-glass friezing temperature (≈120 K) is in good

agreement with our data on Fe-rich amorphous alloys[3,27].

Magnetic properties of three dimensional Al-based icosahedral quasicrystals are presented in Section 2.3. Two dimensional decagonal, octagonal and dodecagonal alloys have also been known as quasicrystals. However, up to the present date, no practical magnetic quasicrystals have been reported, although some two dimensional quasicrystals exhibit excellent photonic properties[71]. Since quasicrystals are in both covalent and metallic states without lattice periodicity, fundamental properties of these quasicrystals have attracted much attention in the fields of strongly correlated electron and frustration systems.

Imry and Wortis discussed the broadening of the first-order transition due to local fluctuations caused by an intrinsic frozen disorder[45]. The extent of broadening is affected by the size of frozen correlated region measured by the coherence length, accompanied by a spatial distribution of the phase transition field and temperature. Such frozen disorders are easily caused in multi-component materials. Therefore, the Maxwell relation is valid to calculate ΔS_m for metamagnetic $La(Fe_xSi_{1-x})_{13}$. In fact, its magnitude obtained from the Maxwell relation is comparable to that from the Clausius–Clapeyron equation. This model would also explain the Invar characteristics given Figs. 2 and 3 as a complete rounding of the first-order transition of Cr-Fe and Cr-Si alloys by addition of the third element.

Antiferromagnetic spintronics has become an active field of research. Park et al. have demonstrated a large spin-valve-like signal in a NiFe/$Mn_{80}Ir_{20}$/MgO/Pt stack with an antiferromagnet on one side and a nonmagnetic metal on the other side of the tunnel barrier. Ferromagnetic moments in NiFe are reversed by external fields of approximately 50 mT or less, and the exchange-spring effect of NiFe on $Mn_{80}Ir_{20}$ γ-phase alloy (see Fig. 7) induces rotation of antiferromagnetic moments, which is detected by the measured tunneling anisotropic magnetoresistance. Their work demonstrates a spintronic element whose transport characteristics are governed by an antiferromagnet[72].

There are four kinds of Heusler-type alloys, i.e., XYZ ($C1_b$), X_2YZ ($L2_1$), inverse Heusler and quaternary Heusler and a number of half metal Heusler alloys have been reported. The structural stability comes to attention from practical viewpoints. The *sp*-elements are not responsible for the existence of the minority gap; whereas, they are nevertheless very important for the physical properties of Heusler alloys because hybridizations of *d–ps* electrons contribute to the bonding state[73]. Therefore, studies on the chemical orbital Hamiltonian population are considered to be important.

Acknowledgements Accomplishing my research described in this article would not have been possible without many supports. I am indebted to all our past collaborators, postdocs, and students, too numerous to list individually. Their contributions are clear from the large number of citations of their work in many bibliographies. I acknowledge the generous financial supports from the Ministry of Education, Culture, Sports, Science, and Technology of Japan and from the Japan Science and Technology Agency.

References

1) K. Fukamichi: *Magnetic Properties of Metals* III, 19 I·1 (ed. H. P. J. Wijn, *Landolt-Börnstein* Springer-Verlag, Berlin, 1994), pp. 193-213.
2) K. Fukamichi: *Amorphous Metallic Alloys* (ed by F. E. Luborsky, Butterworths Co. Ltd., London, 1983), pp. 317-340.
3) K. Fukamichi: *Current Topics in Amorphous Materials-Physics and Technology* (eds. by Y. Sakurai, Y. Hamakawa, T. Masumoto and K. Suzuki, North-Holland Pub. Amsterdam,1993), pp. 98-108.
4) K. Fukamichi: *Physical Properties of Quasicrystals* (ed. Z. M. Stadnik, Springer Solid-State Science Series, Berlin,1999), pp.297-326.
5) K. Fukamichi, A. Fujita, T. H. Chiang, E. Matsubara and Y. Waseda: *Structure and Properties of Aperiodic Materials* (eds. by Y. Kawazoe and Y. Waseda, Springer, Berlin, 2003), pp. 93-200.
6) K. Fukamichi: *Handbook of Advanced Magnetic Materials* (eds. by Y. Liu, J. S. Sellmyer and D. Shindo, Springer, Berlin, 2006), pp. 683-744.
7) A. Sakuma and K. Fukamichi: *Handbook of Advanced Magnetic Material* (eds. by Y. Liu, J. S. Sellmyer and D. Shindo, Springer, Berlin, 2006), pp. 914-975.
8) K. Fukamichi, A. Sakuma, R. Y. Umetsu and C. Mitsumata: *Handbook of Magnetic Materials* **Vol. 16** (ed. by K. H. J. Buschow, Elsevier Science B. V., Amsterdam, 2006), pp. 209-401.
9) E. Fawcett, H. L. Alberts, V. Yu. Galkin, D. R. Noakes and J. V. Yakhmi: *Rev. Mod. Phys.* **66**, 25 (1994).
10) K. Fukamichi and H. Saito: *Sci. Re. RITU* **A26**, 299 (1977).
11) P. A. Fedders and P. C. Martin: *Phys. Rev.* **143**, 245 (1966).
12) S. Komura, Y. Hamaguchi and N. Kunitomi: *J. Phys. Soc. Jpn.* **23**, 171 (1967).
13) Y. Ishikawa, S. Hoshino and Y. Endoh: *J. Phys. Soc. Jpn.* **22**, 1221 (1967).
14) K. Fukamichi and H. Saito: *J. Phys. Soc. Jpn.* **38**, 287 (1975).
15) K. Fukamichi and H. Saito: *Phys. Stat. Sol.* (a) **10**, K129 (1972).
16) K. Fukamichi and H. Saito: *AIP Conf. Proc.* **17**, 45 (1975).
17) K. Fukamichi and H. Saito: *AIP Conf. Proc.* **24**, 384 (1975).
18) K. Fukamichi, H. Hiroyoshi, M. Kukuchi and T. Masumoto: *J. Magn. Magn. Mater.* **10**, 294(1979).
19) E. P. Wohlfarth: *J. Phys. C* **2**, 68 (1969).
20) K. Fukamichi, M. Kikuchi, S. Arakawa, T. Masumoto, T. Jagielinski, K. I. Arai and N. Tsuya: *Solid State Commun.* **27**, 405 (1978).
21) M. Kikuchi, K. Fukamichi and T. Masumoto: *J. Magn. Magn. Mater.* **10**, 300 (1979).
22) V. L. Moruzzi, P. Oelhafen and A. R. Williams: *Phys. Rev. B* **27**, 7194 (1983).
23) A. P. Malozemoff, A. R. Williams, V. L. Moruzzi and K.

Terakura: *Phys. Rev.* B **30**, 6565 (1984).
24) K. Fukamichi and H. Hiroyoshi: *Sci. Rep. RITU* **A32**, 154 (1985).
25) J. Friedel: *Nuovo Cimento* **10**, No. 2, 287 (1958).
26) A. P. Malozemoff, A. R. Williams, K. Terakura, V. L. Moruzzi and K. Fukamichi: *J. Magn. Magn. Mater.* **31-34**, 192 (1983).
27) K. Fukamichi and H. Komatsu: *MRS Int'l Mtg. on Adv. Mats.* **11**, 285 (1989).
28) M. Matsuura, H. Wakabayashi, T. Goto, H. Komatsu and K. Fukamichi: *J. Phys. Condens. Matter* **1**, 2077 (1989).
29) D. Shechtman, I. Blech, D. Gratias and J. W. Chan: *Phys. Rev. Lett.* **53**, 1951 (1984).
30) P. J. Steinhardt, D. R. Nelson and M. Ronchetti: *Phys. Rev. Lett.* **47**, 1297 (1981).
31) P. J. Steinhardt, D. R. Nelson and M. Ronchetti: *Phys. Rev. B* **28**, 784 (1983).
32) D. R. Nelson: *Phys. Rev. B* **28**, 5515 (1983).
33) J. A. Barker, M. R. Hoare and J. L. Finny: *Nature* **257**, 120 (1975).
34) K. Fukamichi, Y. Hattori, H. Nakane and T. Goto: *Mater. Trans.* **34**, 122 (1993).
35) T. Goto, T. Sakakibara and K. Fukamichi: *J. Phys. Soc. Jpn.* **57**, 1751 (1988).
36) K. Fukamichi and T. Goto: *Sci. Rep. RITU* **A36**, 143 (1991).
37) E. P. Wohlfarth and P. Rhodes: *Phil. Mag.* **7**, 1817 (1962).
38) T. Goto, H. A. Katori, T. Sakakibara, H. Mitamura, K. Fukamichi and K. Murata: *J. Appl. Phys.* **76**, 6682 (1994).
39) K. Fukamichi, T. Yokoyama, H. Saito, T. Goto and H. Yamada: *Phys. Rev. B* **64**, 134401 (2001).
40) T. Moriya: *Spin Fluctuations in Itinerant Electron Magnetism*, (Springer-Verlag, Berlin, 1985).
41) A. M. van der Kraan, K. H. J. Buschow and T. T. M. Palstra: *Hyperfine Interact.* **15-16**, 717(1983).
42) K. Irisawa, A. Fujita, K. Fukamichi, M. Yamada, H. Mitamura and T. Goto: *Phys. Rev. B* **70**, 214405 (2004).
43) A. Fujita, Y. Akamatsu and K. Fukamichi: *J. Appl. Phys.* **85**, 4756 (1999).
44) A. Fujita, S. Fujieda, Y. Hasegawa and K. Fukamichi: *Phys. Rev. B* **67**, 104416 (2003).
45) Y. Imry and M. Wortis: *Phys. Rev. B* **19**, 3580 (1979).
46) S. Fujieda, A. Fujita, N. Kawamoto and K. Fukamichi: *Appl. Phys. Lett.* **89**, 062504 (2006).
47) A. Fujita, S. Fujieda, K. Fukamichi, H. Mitamura and T. Goto: *Phys. Rev. B* **65**, 014410 (2001).
48) H. Yamada and K. Terao: *J. Phys. Condens. Matter* **6**, 10805 (1994).
49) S. Fujieda, A. Fujita, K. Fukamichi, Y. Yamasaki and Y. Iijima: *Appl. Phys. Lett.* **79**, 653(2001).
50) R. Y. Umetsu, C. Mitsumata, A. Sakuma and K. Fukamichi: *Trans. Magn. Jpn.* **3**, 59 (2003).
51) R. Y. Umetsu, K. Fukamichi and A. Sakuma: *Mater. Trans.* **47**, 2(2006).
52) W. Kohn and L. J. Sham: *Phys. Rev.* **140**, A1133 (1965).
53) C. Mitsumata, A. Sakuma and K. Fukamichi: *Phys. Rev. B* **68**, 014437 (2003).
54) M. W. Long: *J. Phys. Condens. Matter* **1**, 2857 (1989).
55) I. Žutić, J. Fobian and S. D. Sarma: *Rev. Mod. Phys.* **76**, 323 (2004).
56) J. M. D. Coey and M. Venkatesan: *J. Appl. Phys.* **91**, 8345 (2002).
57) R. Y. Umetsu, K. Kobayashi, A. Fujita, K. Fukamichi, A. Sakuma, R. Kainuma and K. Ishida: *Appl. Phys. Lett.* **85**, 2011 (2004).
58) R. Y. Umetsu, K. Kobayashi, A. Fujita, K. Oikawa, R. Kainuma, K. Ishida, K. Fukamichi and A. Sakuma: *Phys. Rev. B* **72**, 214412 (2005).
59) K. Kobayashi, R. Kainuma, K. Ishida, R.Y. Umetsu, T. Oyamada, A. Fujita and K. Fukamichi: *Appl. Phys. Lett.* **85**, 4684 (2004).
60) K. Ulakko, J. K. Huang, C. Kantner, R. C. O'Handley and V. V. Kokorin: *Appl. Phys. Lett.* **69**, 1966 (1996).
61) R. C. O'Handley: *J. Appl. Phys.* **83**, 3263 (1998).
62) H. Morito, K. Oikawa, A. Fugita, K. Fukamichi, R. Kainuma and K. Ishida: *Scripta Mater.* **63**, 379 (2010).
63) K. Oikawa, L. Wulff, T. Iijima, F. Gejima, T. Ohmori, A. Fujita, K. Fukamichi, R. Kainuma and K. Ishida: *Appl. Phys. Lett.* **79**, 3290 (2001).
64) H. Morito, A. Fujita, K. Fukamichi, R. Kainuma, K. Ishida and K. Oikawa: *Appl. Phys. Lett.* **81**, 1657 (2002).
65) H. Morito, A. Fujita, K. Oikawa, K. Ishida, K. Fukamichi and R. Kainuma: *Appl. Phys. Lett.* **90**, 062505 (2007).
66) H. Morito, K. Oikawa, A. Fujita, K. Fukamichi, R. Kainuma and K. Ishida:*J. Alloys and Compd.* **577S**, S372-S375(2013).
67) H. Morito, K. Oikawa, A. Fujita, K. Fukamichi, R. Kainuma and K. Ishida: *J. Phys. Condens. Matter* **21**, 256002 (2009).
68) A. J. A. de Oliveira and P. C. de Camargo: *Handbook of Advanced Magnetic Material* (eds. by Y. Liu, J. S. Sellmyer and D. Shindo, Springer, Berlin, 2006), pp. 159-210.
69) D. T. Pierce, J. Unguris, R. J. Gelotta and M. D. Stiles: *J. Magn. Magn. Mater.* **200**, 290 (1999).
70) K. Kakehashi: *Phys. Rev. B* **41**, 9207 (1990).
71) M. E. Zoorob, M. D. B. Charlton, G. J. Parker, J. J. Baumberg and M. C. Netti: *Nature* **404**, 740 (2000).
72) B. G. Park, J.Wunderlich, X. Martí, V. Holý, Y. Kurosaki, M. Yamada, H. Yamamoto, A. Nishide, J. Hayakawa, H. Takahashi, A. B. Shick and T. Jungwirth: *Nature Mater.* **10**, 347 (2011).
73) K. Ramesha, R. Seshadri, C. Ederer, T. He and M. A. Subramanian: *Phys. Rev. B* **70**, 214409 (2004).

Received March 5, 2017; Accepted May 15, 2017

J. Magn. Soc. Jpn., **41**, 94-98 (2017)

<Paper>

Synthesis of non-magnetic-ion-substituted Ca-based M-type ferrite

M. Shigemura, K. Kakizaki, and K. Kamishima

Graduate School of Science and Engineering, Saitama University, *255 Shimo-okubo, Sakura-ku, Saitama, Japan*

We investigated the synthesis conditions and magnetic properties of non-magnetic-ion-substituted Ca-based hexagonal ferrites, $Ca_{0.8}La_{0.2}Fe_{8.0-2x}Mg_xTi_xO_{19-\sigma}$ (x = 0.1–3.5) and $Ca_{0.8}La_{0.2}Fe_{y-x}Al_xO_{19-\sigma}$ (x = 1.0–5.0, y = 8.0–10). We found that Mg-Ti-substituted Ca-based M-type ferrites formed at x = 0.1 and 0.2 at above 1225°C. The sample at x = 0.1 showed the crystallographic single phase of M-type ferrite. The minimum Curie temperature of the Mg-Ti-substituted samples was 367°C. Also, we found that the Al-substituted Ca-based M-type ferrites had the main phase of M-type ferrite in all samples. As the amount of substituted Al increased, the saturation magnetization and the Curie temperature decreased, and the coercivity increased. As the amount of substituted Al increased by Δx = 1, the Curie temperature decreased by ΔT_C = 50–70°C. Al-substituted samples of x = 1.0 and 2.0 sintered at 1300°C had the single phase of M-type ferrite.

Keywords: hexagonal ferrites, M-type, calcium compound, non-magnetic ions, Mg-Ti, Al

1. Introduction

M-type ferrite is a type of hexagonal ferrite. Its chemical formula is expressed as $M^{2+}Fe^{3+}{}_{12}O_{19}$ (M^{2+}=Ba^{2+}, Sr^{2+}). The M-type ferrite has high saturation magnetization and high coercivity and is mainly used as a permanent magnet. The Curie temperatures of $BaFe_{12}O_{19}$ and $SrFe_{12}O_{19}$ are 450°C and 460°C, respectively.[1)–4)] It is also possible to tune the magnetic properties of the pure M-type ferrites by the substitution of non-magnetic ions such as Mg^{2+}-Ti^{4+}, Zn^{2+}-Ti^{4+}, and Al^{3+}.[5)–10)]

On the other hand, we had investigated the synthesis conditions of Ca-based M-type ferrite in our previous study.[11)] In the study, the sintering temperature of the highest magnetization sample was 1250°C and the analyzed composition was approximately Ca:La:Fe = 0.8:0.2:9.0. The saturation magnetization of the sample was 68.0 Am²/kg at room temperature and 104 Am²/kg at 5 K (−268°C). The Curie temperature of this sample was about 400°C.

In this study, we investigated the synthesis conditions and magnetic properties of non-magnetic-ion-substituted Ca-based M-type ferrites. The substitution of non-magnetic ions for Fe^{3+} can decrease the Curie temperature of a ferrite, which gives the opportunity for new application. For instance, Shimizu *et al.* put forward the non-magnetic-ion-substituted spinel ferrites with relatively low Curie temperatures as the implant material for the magnetic induction hyperthermia therapy.[12)-13)]

We employed Mg^{2+}-Ti^{4+} and Al^{3+} as non-magnetic substituting elements in the Ca-based M-type ferrite. The resources of these elements are rich as well as those of Ca and Fe.[14)] Also, Ca, Mg, Ti, and Al are less toxic than Ba, which is helpful in terms of producing a safer material.

2. Experimental Procedure

Samples were prepared by a conventional ceramic method. We used $CaCO_3$, La_2O_3, α-Fe_2O_3, and (MgO, TiO_2) or Al_2O_3 as starting materials. They were mixed in a desired proportion, $Ca_{0.8}La_{0.2}Fe_{8.0-2x}Mg_xTi_xO_{19-\sigma}$ (x = 0.1–3.5), or $Ca_{0.8}La_{0.2}Fe_{y-x}Al_xO_{19-\sigma}$ (x = 1.0–4.0, y = 8.0–10). The powder was ball-milled for 24 h. The mixed powder was pressed into a pellet shape and pre-calcined in air at 900°C. The sintered sample was pulverized in a mortar and then milled into fine powder with a planetary ball mill (Fritsch, P-7 Premium line with 1 mmϕ zirconia balls and a 45 ml zirconia container) for 10 min. at 1100 rpm. The processed powder was dried and then pressed into disks. The disks were sintered at T_S = 1200–1300°C for 5 h. The crystal structure of the

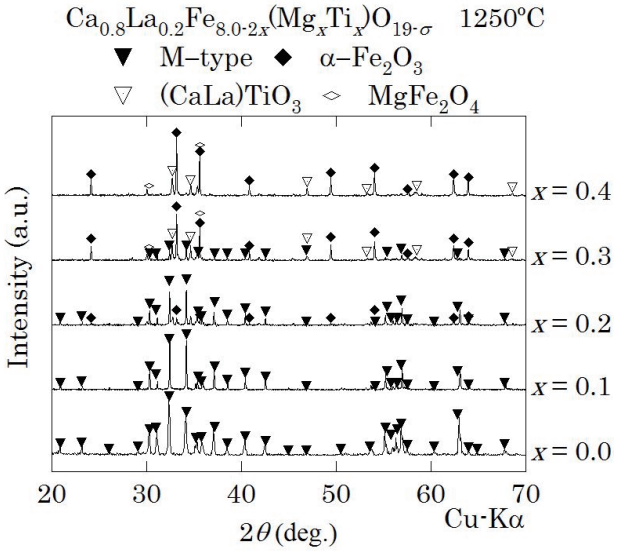

Fig. 1 X-ray diffraction patterns of $Ca_{0.8}La_{0.2}Fe_{8.0-2x}Mg_xTi_xO_{19-\sigma}$ (x = 0.0–0.4) sintered at 1250°C.

sample was examined by powder X-ray diffraction (XRD) analysis with Cu-Kα radiation. The magnetization was measured with a vibrating sample magnetometer (Tamakawa TM-VSM2130HGC) and a superconducting quantum interference device (SQUID) magnetometer (Quantum Design MPMS-XL). The composition was analyzed by the use of an Energy Dispersive X-ray spectrometry (EDX). Here, the composition of oxygen was not examined because the analyses of light elements are less accurate than those of heavy elements.

3. Results and discussion

3-1 Mg-Ti substituted Ca-based M-type ferrite

Figure 1 shows the X-ray diffraction patterns of $Ca_{0.8}La_{0.2}Fe_{8.0-2x}Mg_xTi_xO_{19-\sigma}$ (x = 0.0–0.4) sintered at 1250°C. The main phase is M-type ferrite for the samples with $x \leq 0.2$. The sample at $x = 0.2$ also showed the minority α-Fe_2O_3 phase. The sample at $x = 0.3$ was made up of the mixed phases of α-Fe_2O_3, M-type ferrite, $MgFe_2O_4$, and (CaLa)TiO_3. The samples at $x \geq 0.4$ consisted of α-Fe_2O_3, $MgFe_2O_4$, and (CaLa)TiO_3 phases, but didn't contain M-type ferrite phase. The chemical composition of the perovskite compound of (CaLa)TiO_3 can be various forms such as $Ca_{0.2}La_{0.53}TiO_3$, $Ca_{0.4}La_{0.4}TiO_3$, and $Ca_{0.12}La_{0.58}TiO_3$.[15, 16] It is difficult to determine the chemical composition exactly because the lattice constant of (CaLa)TiO_3 is similar to that of $CaTiO_3$. Since Ca and La cations became starting materials to form the perovskite compounds, M-type ferrite was not formed.

Figure 2 shows the room-temperature saturation magnetization of $Ca_{0.8}La_{0.2}Fe_{8.0-2x}Mg_xTi_xO_{19-\sigma}$ (x = 0.0–0.4) sintered at 1200–1300°C. Here, the saturation magnetization of the sample at $x = 0.0$ is that of sample prepared with the optimum preparation conditions in the previous study.[11] The saturation magnetization decreased with increasing the amount of Mg-Ti substitution. The gradual decrease of the magnetization indicated the formation of Mg-Ti substituted M-type ferrite at $x = 0.1$ and 1225°C ≤ T_S ≤ 1250°C. The substitution of non-magnetic Mg^{2+} and Ti^{4+} for magnetic Fe^{3+} can decrease total magnetic moment. Even at the same substitution rate of x=0.1, however, the samples with T_S=1200°C and 1300°C showed low magnetizations. The decrease of the magnetization was more obvious at x=0.2 and T_S≥1225°C in spite that the main phase was the M-type phase. It should be noted that the synthesis condition of Ca-based M-type ferrite is so delicate that the M-type structure can easily be broken.[11] Since the sample at $x = 0.2$ and T_S = 1200°C didn't contain M-type ferrite phase, the saturation magnetization became much smaller than those of the $x = 0.2$ samples with higher sintering temperatures.

Figure 3 shows the temperature dependence of magnetization of $Ca_{0.8}La_{0.2}Fe_{8.0-2x}Mg_xTi_xO_{19-\sigma}$ at $0.0 \leq x \leq 0.2$. The Curie temperature decreased with increasing the amount of Mg-Ti substitution. The non-magnetic

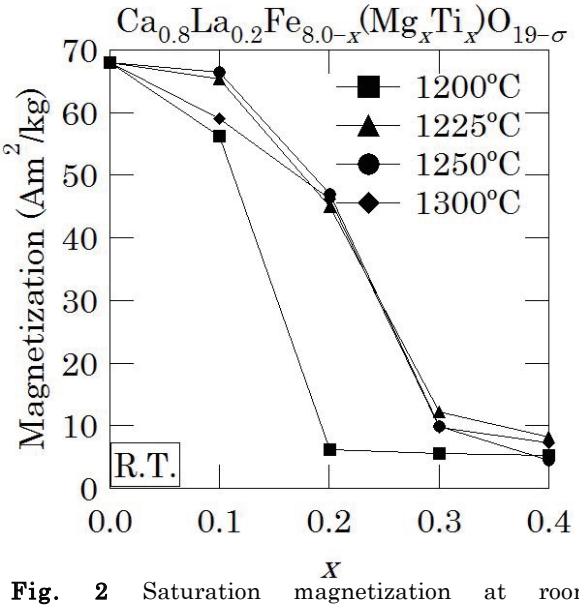

Fig. 2 Saturation magnetization at room temperature of $Ca_{0.8}La_{0.2}Fe_{8.0-2x}Mg_xTi_xO_{19-\sigma}$ (x = 0.0–0.4) sintered at 1200, 1225, 1250°C and 1300°C.

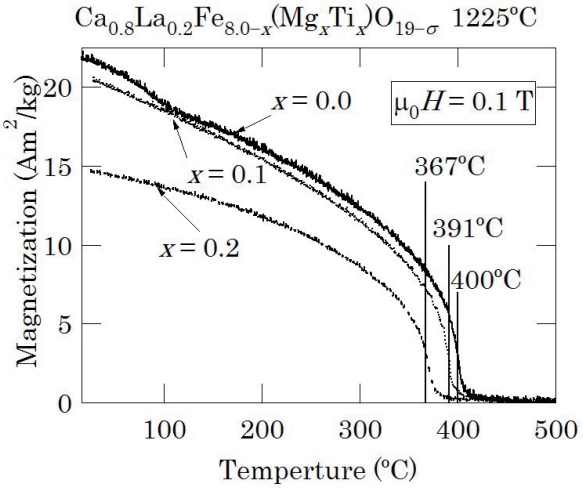

Fig. 3 Temperature dependence of magnetization of $Ca_{0.8}La_{0.2}Fe_{8.0-2x}Mg_xTi_xO_{19-\sigma}$ (x = 0.1 and 0.2) sintered at 1225°C and x = 0.0 sintered at 1250°C.

Mg^{2+} and Ti^{4+} ions decrease the number of the connection between magnetic iron ions (Fe^{3+}–O^{2-}–Fe^{3+}) in Mg-Ti substituted Ca-based M-type ferrite at $x \leq 0.2$.

3-2 Al substituted Ca-based M-type ferrite

Figure 4 shows X-ray diffraction patterns of $Ca_{0.8}La_{0.2}Fe_{8.0-x}Al_xO_{19-\sigma}$ (x = 1.0–4.0) sintered at 1250°C. The main phase is M-type ferrite for these samples although minority phases of $CaFe_4O_7$ and $CaAl_4O_7$ are also observed. The formation of $CaFe_4O_7$ can be caused by the deficiency of Fe cations to form the M-type structure. Therefore, we attempted to increase the amounts of (Fe+Al)/(Ca+La) to 10.

Figure 5 shows X-ray diffraction patterns of

$Ca_{0.8}La_{0.2}Fe_{10-x}Al_xO_{19-\sigma}$ (x = 1.0–4.0) sintered at 1300°C. The samples of x = 1.0 and 2.0 are in the single phase of M-type ferrite, but the samples of x = 3.0 and 4.0 have the main M-type ferrite phase and the minority $CaFe_4O_7$ phase. Here, it should be noted that high temperature sintering is necessary for formation of $CaAl_{12}O_{19}$.[17] Actually, Nagumo *et al.* reported that iron-substituted hibonite ($CaAl_{12-x}Fe_xO_{19}$) samples were synthesized at a relatively low sintering temperature of 1300°C as the amount of Al was decreased.[18] Therefore, it is possible that the substitution of Al may increase the suitable sintering temperature to form the single M-type phase. Also, the diffraction peaks of M-type phase shifted to the higher angle side as the substitution amount increased. Table 1 shows the ionic radii of Fe^{3+} and Al^{3+}.[19] Since Al^{3+} is smaller than Fe^{3+}, the lattice constants decrease with increasing the amount of Al^{3+}, as shown in Fig. 6. Therefore, the Al-substituted M-type ferrite was formed successfully.

Figure 7 shows the saturation magnetization and the coercivity at room temperature of

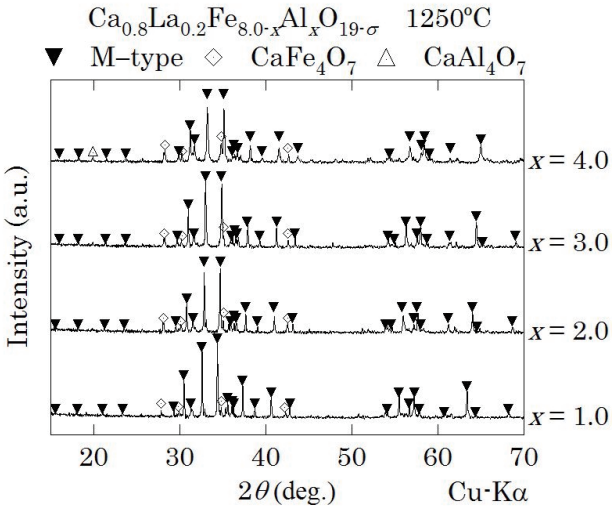

Fig. 4 X-ray diffraction patterns of $Ca_{0.8}La_{0.2}Fe_{8.0-x}Al_xO_{19-\sigma}$ (x = 1.0–4.0) sintered at 1250°C.

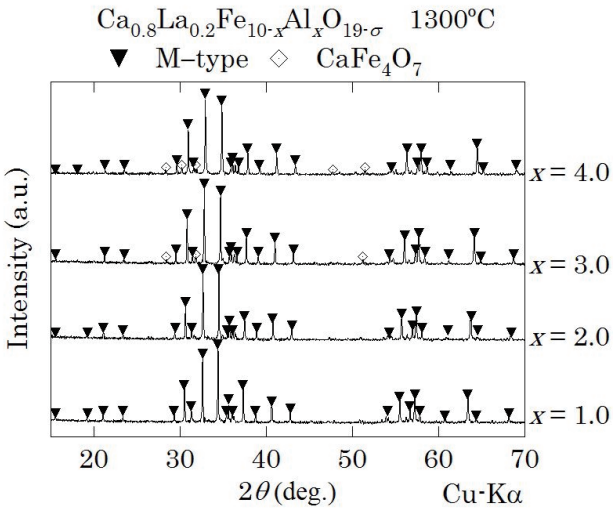

Fig. 5 X-ray diffraction patterns of $Ca_{0.8}La_{0.2}Fe_{10-x}Al_xO_{19-\sigma}$ (x = 1.0–4.0) sintered at 1300°C.

Table 1 Ionic radii of each coordination number of Fe and Al.

	Octahedral	Tetrahedral	Trigonal bipyramidal
Fe^{3+} (Å)	0.645	0.49	0.58
Al^{3+} (Å)	0.535	0.39	0.48

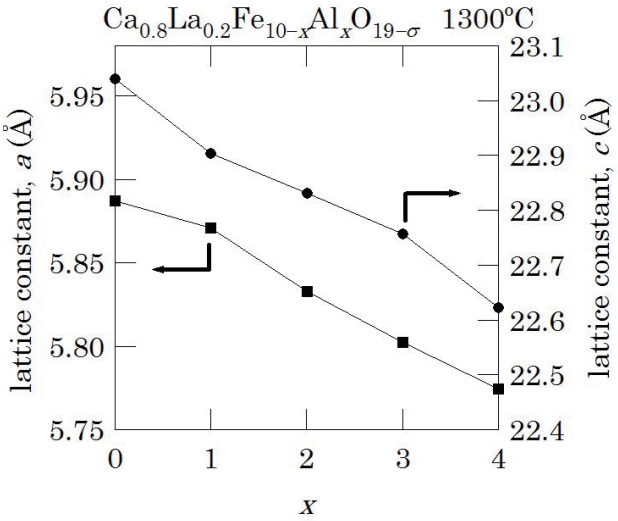

Fig. 6 Lattice constant of $Ca_{0.8}La_{0.2}Fe_{10-x}Al_xO_{19-\sigma}$ (x = 1.0–4.0) sintered at 1300°C.

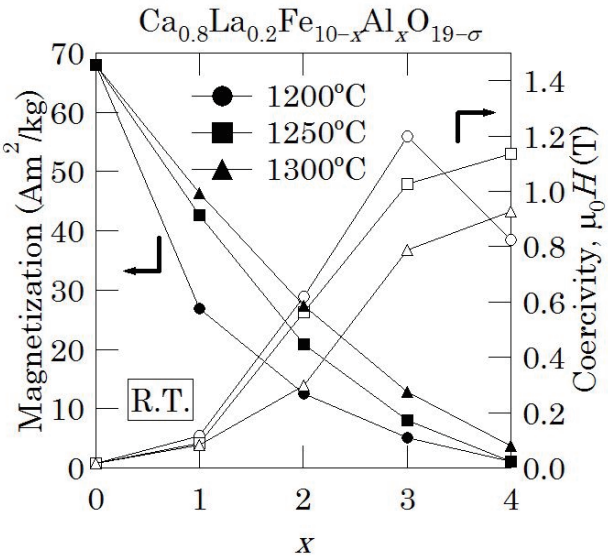

Fig. 7 Saturation magnetization and coercivity at room temperature of $Ca_{0.8}La_{0.2}Fe_{10-x}Al_xO_{19-\sigma}$ (x = 1.0–4.0) sintered at 1200-1300°C.

$Ca_{0.8}La_{0.2}Fe_{10-x}Al_xO_{19-\sigma}$ (x = 1.0–4.0) sintered at 1200–1300°C. The saturation magnetization decreased and the coercivity increased with increasing amount of Al. The decrease of the saturation magnetization at room temperature is caused by the substitution of non-magnetic ions (Al^{3+}) for magnetic ions (Fe^{3+}), which can decrease the intrinsic magnetic moment and the Curie temperature.

In contrast, the Al substitution increased the coercivity of the Ca-based M-type ferrite although the coercivity of the starting sample without Al was small.[11] The Al-substitution effect on coercivity is similar to those of other M-type ferrites. For instance, Haneda and Kojima reported that $BaAl_xFe_{12-x}O_{19}$ exhibited a large increase in coercivity and that the magnetocrystalline anisotropy field contributed greatly to the increase of coercivity.[20] De Bitetto also found that the anisotropy field of $SrO \cdot xAl_2O_3 \cdot (6-x)Fe_2O_3$ increased as the substitution amount of Al (x) was increased.[21]

The Al-substitution effects on coercivity of M-type ferrites have been attributed to the variation of magnetocrystalline anisotropy under the assumption of a single-domain model (Stoner-Wohlfarth model).[8,10,20–21] This assumption is plausible because the single-domain structure can be stabilized by the reduction of magnetostatic energy if the decrease of the saturation magnetization is more significant than the change of the magnetocrystalline anisotropy.[22–23] According to the Stoner-Wohlfarth model, the coercivity can be expressed as

$$H_C \propto K_1/M_S$$

where H_C is the coercivity, K_1 is the magnetocrystalline uniaxial anisotropy constant, and M_S is the saturation magnetization. If the decrease of K_1 is smaller than the decrease of M_S, H_C can be increased. The studies of Al substituted Sr-based M-type ferrite also showed that the saturation magnetization decreased and the coercivity increased with increasing amount of Al.[8–10, 21] This tendency is consistent with our result.

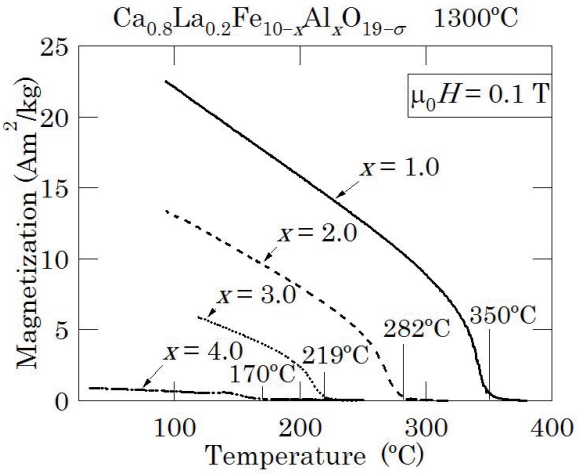

Fig. 8 Temperature dependence of magnetization of $Ca_{0.8}La_{0.2}Fe_{10-x}Al_xO_{19-\sigma}$ (x = 1.0–4.0) sintered at 1300°C.

Figure 8 shows the temperature dependence of magnetization of $Ca_{0.8}La_{0.2}Fe_{10-x}Al_xO_{19-\sigma}$ (x = 1.0–4.0) sintered at 1300°C. The Curie temperature of these samples decreased with increasing the amount of Al. As the Al substitution increased by Δx = 1, the Curie temperature decreased by ΔT_C = 50–70°C. The substitution of the non-magnetic Al^{3+} for Fe^{3+} causes to decrease the links of Fe^{3+}–O^{2-}–Fe^{3+}, and consequently weakens the superexchange interaction in the M-type structure.

Figure 9 shows the magnetization curves at 5 K (−268°C) of $Ca_{0.8}La_{0.2}Fe_{10-x}Al_xO_{19-\sigma}$ (x = 1.0 and 2.0) sintered at 1300°C. The saturation magnetic moment per molecule at x = 1.0 is estimated to be 12.5 μ_B/f.u. from the magnetization at μ_0H=7 T (85.0 Am²/kg). The EDX analysis showed the chemical formula of this sample as $Ca_{0.88}La_{0.12}Fe_{8.80}Al_{1.01}O_{15.8}$. Here, the composition ratio of oxygen is estimated from the charge balance with the concentration of Ca^{2+}, La^{3+}, Fe^{3+}, and Al^{3+} cations.

The saturation magnetic moment per molecule at x = 2.0 is also estimated to be 7.86 μ_B/f.u. from the magnetization at μ_0H=7 T (55.1 Am²/kg). The EDX analysis of this sample showed the chemical formula of $Ca_{0.83}La_{0.17}Fe_{7.88}Al_{1.83}O_{15.7}$.

Comparing these two results, the difference of the magnetic moment between these two samples is 4.7 μ_B, which is approximately close to the magnetic moment of Fe^{3+} (5 μ_B). In other words, as the substitution amount of Al^{3+} increased by 1, one Fe^{3+} located at the up spin sites decreased. In other words, Al^{3+} prefers to be located at the up spin sites. Therefore, the saturation magnetization was greatly decreased even by the small amount of Al substitution.

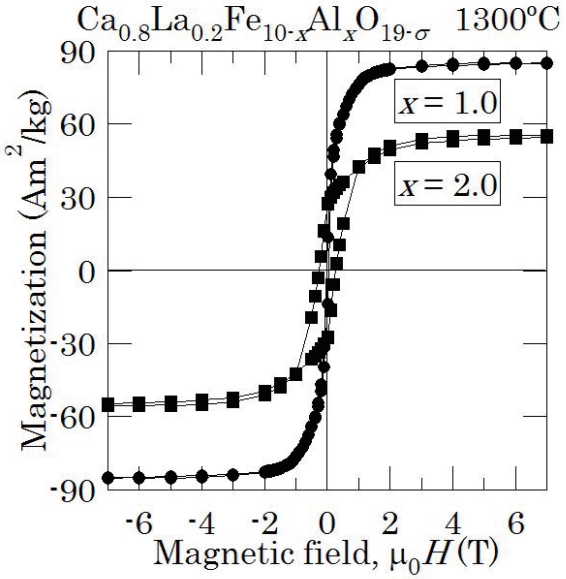

Fig. 9 Magnetization curves at 5 K (−268°C) of $Ca_{0.8}La_{0.2}Fe_{10-x}Al_xO_{19-\sigma}$ (x = 1.0 and 2.0) sintered at 1300°C.

4. Conclusion

We have investigated the synthesis conditions and magnetic properties of non-magnetic-ion-substituted Ca-based M-type ferrites. In the Mg-Ti substitution case of $Ca_{0.8}La_{0.2}Fe_{8.0-2x}Mg_xTi_xO_{19-\delta}$, the single-phase sample was formed at x = 0.1. As the amount of substitution increased, both the saturation magnetization and the Curie temperature decreased. In the Al substitution case of $Ca_{0.8}La_{0.2}Fe_{y-x}Al_xO_{19-\delta}$, samples, the single M-type phase samples were formed at x = 1.0 and 2.0 sintered at 1300°C. As the amount of substituted Al increased, the saturation magnetization and the Curie temperature decreased and the coercivity increased. The Al substitution seems to change the distribution of iron cations in the M-type structure and to cause to change the magnetic properties.

References

1) J. Smit and H. P. J. Wijn: Ferrites, pp. 182–184, pp. 193–194 (Philips Technical Library, Netherlands 1959).
2) S. Chikazumi: Physics of Ferromagnetism, p. 212 (Oxford University Press, Oxford, 2009).
3) G. W. Rathenau: *Rev. Mod. Phys.*, **25**, 297 (1953).
4) Ü. Özgür, Y. Alivov, and H. Morkoc: *J. Mater. Sci-Mater. El.*, **20**, 789 (2009).
5) S. Alablance, J. Thery, and D. Viven: *Mater. Res. Bull.*, **24**, 475 (1989)
6) V. V. Soman, V. M. Nanoti, and D. K. Kulkarni: *Ceram. Int.*, **39**, 5713 (2013).
7) V. V. Soman, V. M. Nanoti, D. K. Kulkarni, and V. V. Soman: *Physics Procedia*, 54, 30 (2014).
8) M. Liu, X. Shen, F. Song, J. Xiang, and X. Meng: *J. Solid State Chem.*, 184, 871 (2011).
9) H. Z. Wang, B. Yao, Y. Xu, Q. He, G. H. Wen, S. W. Long, J. Fan, G. D. Li, L. Shan, B. Liu, L. N. Jiang, and L. L. Gao: *J. Alloy. Compd.*, **537**, 43 (2012).
10) H. Luo, B. K. Rai, S. R. Mishra, V. V. Nguyen, J. P. Liu: *J. Magn. Magn. Mater.*, **324**, 2602 (2012).
11) M. Shigemura, K. Watanabe, K. Kakizaki, and K. Kamishima: *J. Magn. Soc. Jpn*, **41**, 10 (2017).
12) T. Shimizu, M. Matsui: *Sci. Technol. Adv. Mater.*, **4**, 469 (2003).
13) T. Shimizu, H. Asano, M. Matsui: *J. Magn. Magn. Mater.*, **310**, 1835 (2007).
14) F. W. Clarke and H. S. Washington: The Composition of the Earth's Crust, pp. 20–21 (United States Geological Survey, Washington, 1924).
15) Z. Zhang, G. R. Lumpkin, C. J. Howard, K. S. Knight, K. R. Whittle, and K. Osaki: *J. Solid State Chem.*, 180, 1083 (2007).
16) The Powder Diffraction File (PDF00-055-0922) by the Internal Center for Diffraction Data (ICDD): L. Vasylechko, Semiconductor Electronic Dept., L`viv Polytechic Natinal Univ., Ukraine. ICDD Grant-in-Aid, (2016).
17) H. H. Mao, M. Selleby, and B. Sundman: *CALPHAD*, **28**[3], 307 (2004).
18) H. Nagumo, K. Watanabe, K. Kakizaki, and K. Kamishima: *J. Magn. Soc. Jpn*, **41**, 20 (2017).
19) R. D. Shannon: *Acta Cryst.* , **A32**, 751 (1976).
20) K. Haneda and H. Kojima: *Jpn. J. Appl. Phys.*, **12**, 355 (1973).
21) D. J. De Bitetto: *J. Appl. Phys.*, **35**, 3482 (1964).
22) *Ibid.* 1, p. 68.
23) *Ibid.* 2, p. 455.

Received Apr. 19, 2017; Accepted Jul. 7, 2017

J. Magn. Soc. Jpn., **41**, 99-107 (2017)

<Paper>

Structure Analysis of Fe-Co and Fe-Co-B Alloy Thin Films Formed on MgO(001) Substrate

Kana Serizawa[1], Mitsuru Ohtake[1,2], Masaaki Futamoto[1], Fumiyoshi Kirino[3], and Nobuyuki Inaba[4]

[1]Faculty of Science and Engineering, Chuo University, *1-13-27 Kasuga, Bunkyo-ku, Tokyo 112-8551, Japan*
[2]Faculty of Engineering, Kogakuin University, *2655-1 Nakano, Hachioji, Tokyo 192-0015, Japan*
[3]Graduate School of Fine Arts, Tokyo University of the Arts, *12-8 Ueno-Koen, Taito-ku, Tokyo 110-8714, Japan*
[4]Faculty of Engineering, Yamagata University, *4-3-16 Jyonan, Yonezawa, Yamagata 992-8510, Japan*

Fe-Co and Fe-Co-B alloy films of 40 nm thickness are prepared by sputtering on MgO(001) single-crystal substrates using alloy targets of $(Fe_{0.7}Co_{0.3})_{100-x}B_x$ (x = 0, 5, 10, 15 at. %) by varying the substrate temperature from room temperature (RT) to 600 °C. The film structure is investigated by reflection high-energy electron diffraction and out-of-plane, in-plane, and pole-figure X-ray diffractions. Preparation condition of epitaxial film is found to depend on the B content and the substrate temperature. Epitaxial $(Fe_{0.7}Co_{0.3})_{100-x}B_x$ films are obtained at the investigated temperatures for the B contents lower than 5 at. %, whereas films with the B contents of 10 and 15 at. % grow epitaxially at temperatures higher than 400 and 600 °C, respectively. Single-crystal films of bcc(001) orientation are formed at temperatures higher than RT, 200, 400, and 600 °C for the B contents of 0, 5, 10, and 15 at. %, respectively. As the substrate temperature decreases, the epitaxial films with B contents of 5–15 at. % tend to involve four types of bcc(122) variant whose orientations are rotated around the film normal by 90° each other. The $(Fe_{0.7}Co_{0.3})_{90}B_{10}$ film deposited at RT and the $(Fe_{0.7}Co_{0.3})_{85}B_{15}$ films deposited at temperatures from RT to 200 °C are found to be consisting of bcc polycrystal and amorphous, respectively. The structure is thus determined to vary in the order of bcc(001) single-crystal => bcc(001) and bcc(122) epitaxial crystals => bcc polycrystal => amorphous with increasing the B content and with decreasing the substrate temperature. The lattices of single-crystal Fe-Co (x = 0 at. %) and Fe-Co-B (x = 5–15 at. %) films are respectively expanded along the in-plane and the perpendicular directions. The single-crystal Fe-Co films show in-plane magnetic anisotropies with the easy magnetization directions of bcc[100] and bcc[010], which is reflecting the magnetocrystalline anisotropy of bulk bcc-$Fe_{70}Co_{30}$ alloy. On the contrary, the single-crystal Fe-Co-B films show almost isotropic in-plane magnetic properties and weak perpendicular anisotropies, which is possibly caused by an influence of lattice deformation along the perpendicular direction.

Key words: Fe-Co alloy, Fe-Co-B alloy, thin film, epitaxial growth, MgO single-crystal substrate, lattice strain, magnetic anisotropy

1. Introduction

Magnetic tunnel junctions consisting of tunnel barrier and ferromagnetic electrode layers have been studied for applications to tunnel magnetoresistance (TMR) sensors and magnetoresistive random access memory devices. In order to achieve high TMR ratios, highly-oriented polycrystalline[1)] or epitaxial single-crystal[2)] MgO layer of (001) orientation is useful as the barrier layer.

Fe-Co and Fe-Co-B alloys with bcc structure are typical soft magnetic materials with high saturation magnetizations and have been frequently used as the electrode material. However, the crystallographic structure of Fe-Co-B film is affected by the B content[3,4)] and the formation condition like annealing temperature[5–8)]. Fe-Co-B film with a higher B content deposited at a lower substrate temperature tends to involve amorphous. The magnetic properties are also delicately influenced by the structure. Furthermore, it has been reported that perpendicular magnetic anisotropy is induced in Fe-Co and Fe-Co-B alloy films when the crystal lattice is strained along the perpendicular direction[9–16)].

In order to investigate the basic structural and magnetic properties, it is useful to employ epitaxial films, since the crystallographic orientation can be controlled by the substrate orientation. However, there are few reports on the preparation of Fe-Co-B films on single-crystal substrates by systematically varying the formation condition. In the present study, $(Fe_{0.7}Co_{0.3})_{100-x}B_x$ films are prepared on MgO(001) substrates. The influences of B content and substrate temperature on the structure and the magnetic properties are investigated.

2. Experimental Procedure

A radio-frequency (RF) magnetron sputtering system equipped with a reflection high-energy electron diffraction (RHEED) facility was used for film formation. The base pressures were lower than 4×10^{-7} Pa. Polished MgO(001) substrates were heated at 600 °C for 1 hour to obtain clean surfaces. $(Fe_{0.7}Co_{0.3})_{100-x}B_x$ (x =

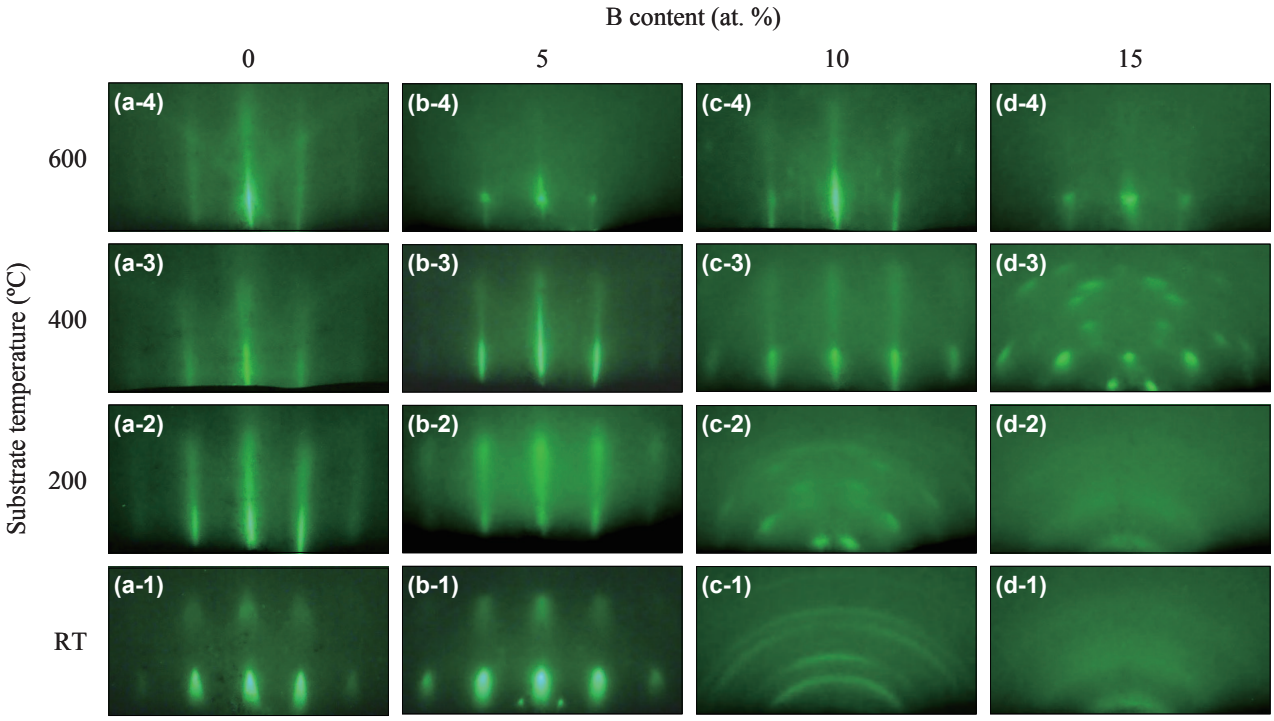

Fig. 1 RHEED patterns observed for $(Fe_{0.7}Co_{0.3})_{100-x}B_x$ films with the B contents of (a) 0, (b) 5, (c) 10, and (d) 15 at. % deposited on MgO(001) substrates at (a-1)–(d-1) RT, (a-2)–(d-2) 200 °C, (a-3)–(d-3) 400 °C, and (a-4)–(d-4) 600 °C. The incident electron beam is parallel to MgO[100].

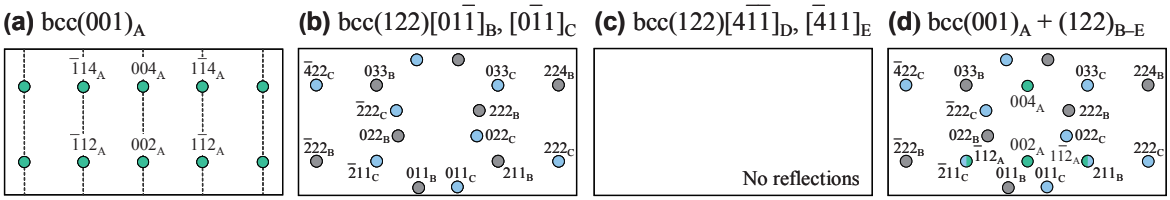

Fig. 2 Schematic diagrams of RHEED patterns simulated for (a) bcc(001) and [(b), (c)] bcc(122) surfaces. Schematic diagram of (d) is drawn by overlapping (a) and (b). The incident electron beam is parallel to (a) bcc(001)[110], (b) bcc(122)[01$\bar{1}$] and [0$\bar{1}$1], or (c) bcc(122)[4$\bar{1}\bar{1}$] and [$\bar{4}$11].

0–15 at. %) alloy targets of 3 inch diameter were employed. The distance between target and substrate was fixed at 150 mm. The Ar gas pressure was kept constant at 0.67 Pa. The RF powers for alloy targets with the B contents of 0, 5, 10, and 15 at. % were respectively adjusted at 57, 65, 60, and 58 W, where the deposition rates were 0.02 nm/s. $(Fe_{0.7}Co_{0.3})_{100-x}B_x$ films of 40 nm thickness were deposited on the substrates at temperatures ranging from RT to 600 °C. In the present study, the film compositions were considered to be similar to the target compositions.

The surface structure was studied by RHEED. The structural properties were investigated by $2\theta/\omega$-scan out-of-plane, $2\theta\chi/\varphi$-scan in-plane, and pole-figure X-ray diffractions (XRDs) with Cu-Kα radiation (λ = 0.15418 nm). The surface morphology was observed by atomic force microscopy (AFM). The magnetization curves were measured at RT by vibrating sample magnetometry.

3. Results and Discussion

3.1 Crystal structure and orientation

Figure 1(a) shows the RHEED patterns of $Fe_{70}Co_{30}$ (x = 0) films deposited on MgO(001) substrates at different temperatures observed by making the incident electron beam parallel to MgO[100]. Diffraction patterns corresponding to bcc(001) single-crystal surface are recognized, as shown in the simulated pattern of Fig. 2(a). The epitaxial orientation relationship is determined as

$$\text{bcc-}(Fe_{0.7}Co_{0.3})_{100-x}B_x(001)[110] \parallel \text{MgO}(001)[100]. \quad \text{(type A)}$$

The $Fe_{70}Co_{30}(001)$ lattice is rotated around the film normal by 45° with respect to the MgO(001) lattice, as shown in Fig. 3. In this configuration, the mismatch between bcc-$Fe_{70}Co_{30}(001)$ crystal and MgO(001)

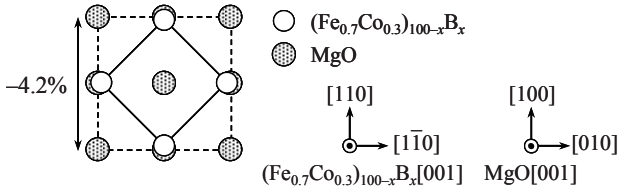

Fig. 3 Planer view schematic diagram of epitaxial orientation relationship of bcc-$(Fe_{0.7}Co_{0.3})_{100-x}B_x$ crystal lattice on MgO(001) substrate.

substrate is calculated by using the lattice constants of bulk $Fe_{70}Co_{30}$ ($a_{Fe70Co30}$ = 0.2858 nm[17]) and MgO (a_{MgO} = 0.4217 nm[18]) crystals to be

$$[(\sqrt{2}\,a_{Fe70Co30} - a_{MgO}) / a_{MgO}] \times 100 = -4.2\%, \quad (1)$$

which suggests a possibility that the bcc-$Fe_{70}Co_{30}$ crystal lattice is expanded along the in-plane direction.

The RHEED patterns observed for $(Fe_{0.7}Co_{0.3})_{95}B_5$ films deposited at 200–600 °C, $(Fe_{0.7}Co_{0.3})_{90}B_{10}$ films deposited at 400–600 °C, and an $(Fe_{0.7}Co_{0.3})_{85}B_{15}$ film deposited at 600 °C are respectively shown in Figs. 1(b-2)–(b-4), (c-3)–(c-4), and (d-4). Diffraction patterns from bcc(001) surface are recognized, similar to the case of $Fe_{70}Co_{30}$ films. $(Fe_{0.7}Co_{0.3})_{100-x}B_x$ single-crystal films of bcc(001) orientation are also obtained for the compositional range of x = 5–15 at. % by using the elevated substrate temperatures.

Figures 1(b-1), (c-2), and (d-3) show the RHEED patterns observed for an $(Fe_{0.7}Co_{0.3})_{95}B_5$ film deposited at RT, an $(Fe_{0.7}Co_{0.3})_{90}B_{10}$ film deposited at 200 °C, and an $(Fe_{0.7}Co_{0.3})_{85}B_{15}$ film deposited at 400 °C, respectively. Diffraction patterns from bcc(122) surface [Fig. 2(b)] are observed in addition to those from bcc(001) surface, as shown in Fig. 2(d). The bcc(122) pattern is analyzed to be an overlap of reflections from two variants, as shown by the indices with subscripts, B and C. The crystallographic orientation relationships are determined as

bcc-$(Fe_{0.7}Co_{0.3})_{100-x}B_x$(122)[01$\bar{1}$] ‖ MgO(001)[100], (type B)

bcc-$(Fe_{0.7}Co_{0.3})_{100-x}B_x$(122)[0$\bar{1}$1] ‖ MgO(001)[100]. (type C)

When the atomic arrangements of MgO(001) and Fe-Co-B(122) surfaces, which are with four- and one-fold symmetries, are considered, bcc(122) variants with the orientation relationships of

bcc-$(Fe_{0.7}Co_{0.3})_{100-x}B_x$(122)[4$\bar{1}\bar{1}$] ‖ MgO(001)[100], (type D)

bcc-$(Fe_{0.7}Co_{0.3})_{100-x}B_x$(122)[$\bar{4}$11] ‖ MgO(001)[100], (type E)

are interpreted to be formed. Figure 2(c) shows the schematic diagram of RHEED pattern simulated for the two bcc(122) variants. When the incident electron beam is parallel to MgO[100] (‖ bcc[4$\bar{1}\bar{1}$] and bcc[$\bar{4}$11]), there

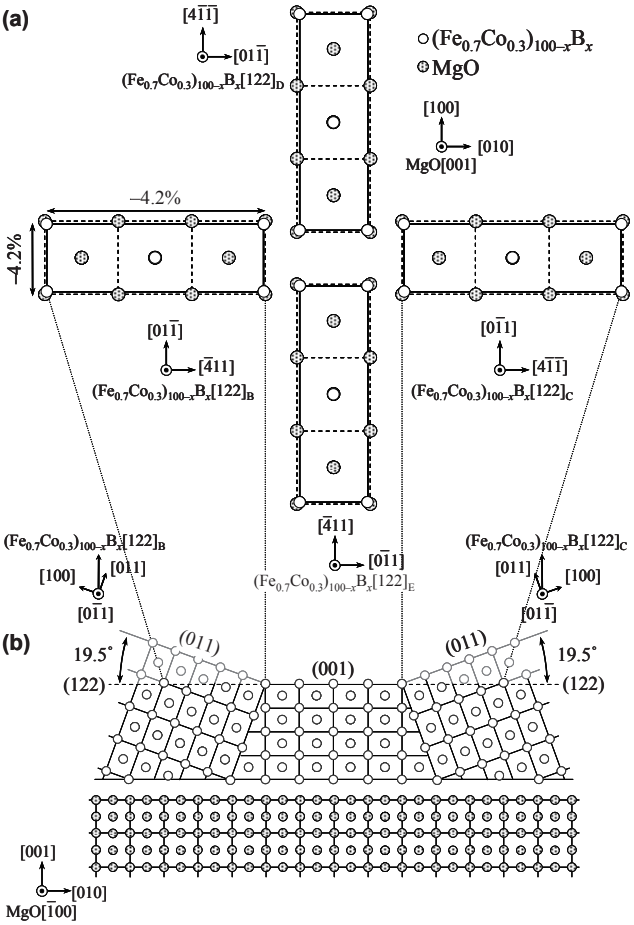

Fig. 4 (a) Planer and (b) cross-sectional view schematic diagrams of epitaxial orientation relationships of bcc-$(Fe_{0.7}Co_{0.3})_{100-x}B_x$(001) crystal and four bcc-$(Fe_{0.7}Co_{0.3})_{100-x}B_x$(122) variants on MgO(001) substrate.

are no reflections in the diffraction pattern. Therefore, the Fe-Co-B films are considered to be consisting of bcc(001) crystal and four bcc(122) variants. The structure is similar to the cases of Fe/GaAs(001)[19] and $Fe_{50}Co_{50}/SrTiO_3$(001)[20] systems. Figure 4 shows the planer and cross-sectional view schematic diagrams of orientation relationships of bcc(001) crystal and four bcc(122) variants. The orientations of bcc(122) variants are rotated around the film normal by 90° each other. The lattice misfit values along bcc[01$\bar{1}$] and bcc[$\bar{4}$11] are respectively calculated to be

$$[(\sqrt{2}\,a_{Fe70Co30} - a_{MgO}) / a_{MgO}] \times 100 = -4.2\%, \quad (2)$$

$$[(3\sqrt{2}\,a_{Fe70Co30} - 3a_{MgO}) / 3a_{MgO}] \times 100 = -4.2\%. \quad (3)$$

The misfit values do not differ depending on the in-plane direction and are the same with the lattice mismatch at the bcc(001)/MgO(001) interface. In order to confirm the orientation relationships, a pole-figure XRD measurement was carried out. Figure 5(a) shows the pole-figure XRD pattern of the $(Fe_{0.7}Co_{0.3})_{85}B_{15}$ film deposited at 400 °C measured by fixing the diffraction

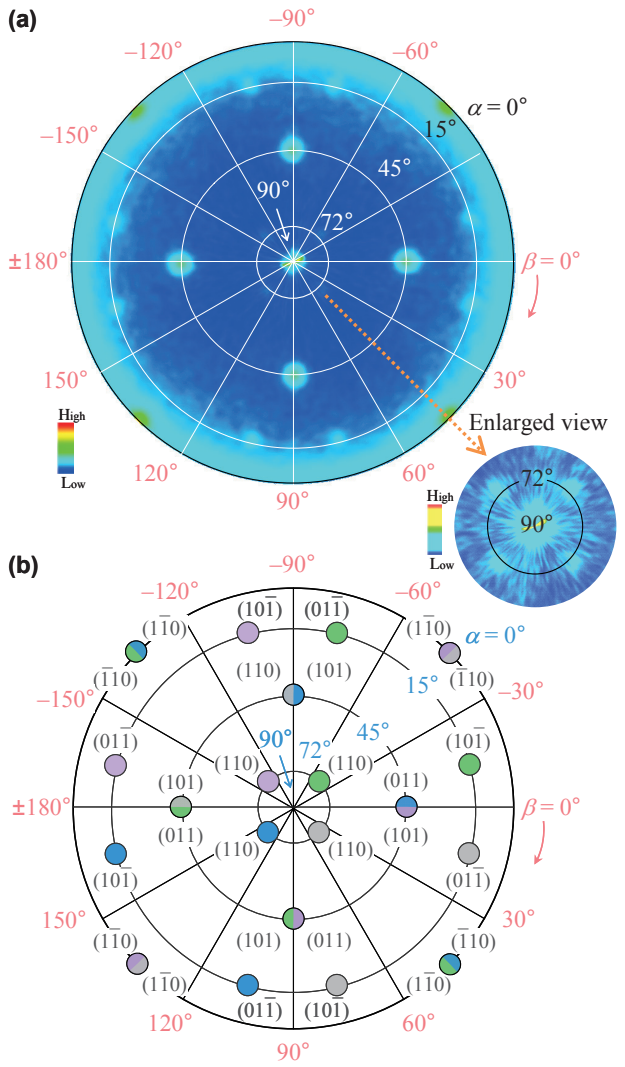

Fig. 5 (a) Pole-figure XRD pattern of $(Fe_{0.7}Co_{0.3})_{85}B_{15}$ film deposited at 400 °C measured by fixing the diffraction angle, $2\theta B$, at 44.5°. The intensity is shown in logarithmic scale. (b) Schematic diagram obtained by overlapping diffraction patterns simulated for the bcc-$(Fe_{0.7}Co_{0.3})_{100-x}B_x$(122) variants grown in the orientation relationships determined by RHEED.

angle, $2\theta B$, at 44.5°, where bcc{110} reflections are expected to be detectable. Figure 5(b) shows the schematic diagram of pole-figure pattern calculated for the four bcc(122) variants. The experimental pole-figure pattern is in agreement with the simulated result. The pole-figure XRD confirms the crystallographic orientation relationships determined by RHEED.

Figure 1(c-1) shows the RHEED pattern observed for an $(Fe_{0.7}Co_{0.3})_{90}B_{10}$ film deposited at RT. A ring-like diffraction pattern is observed. A polycrystalline $(Fe_{0.7}Co_{0.3})_{90}B_{10}$ film is formed. Figures 1(d-1) and (d-2) show the RHEED patterns observed for $(Fe_{0.7}Co_{0.3})_{85}B_{15}$ films deposited at RT and 200 °C, respectively. Halo diffraction patterns are recognized. Amorphous $(Fe_{0.7}Co_{0.3})_{85}B_{15}$ films are formed.

Figure 6 summarizes the structure and

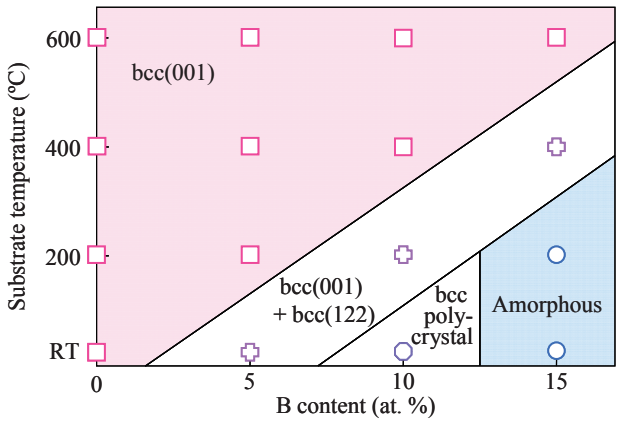

Fig. 6 Phase diagram of $(Fe_{0.7}Co_{0.3})_{100-x}B_x$ film deposited on MgO(001) substrate.

crystallographic orientation of $(Fe_{0.7}Co_{0.3})_{100-x}B_x$ film deposited on MgO(001) substrate. The structure varies in the order from bcc(001) single-crystal, bcc(001) and bcc(122) crystals, bcc polycrystal, and to amorphous with increasing the B content and with decreasing the substrate temperature.

3.2 Lattice strain

Figure 7 shows the out-of-plane and in-plane XRD patterns measured for the $(Fe_{0.7}Co_{0.3})_{100-x}B_x$ films with different B contents deposited at 200 °C. Here, the scattering vector of in-plane XRD is parallel to MgO[1$\bar{1}$0]. As shown in the data of Fig. 6, these four films are consisting of bcc(001) single-crystals (B content: 0, 5 at. %), mixture of bcc(001) and bcc(122) crystals (B content: 10 at. %), and amorphous (B content: 15 at. %), respectively. Strong out-of-plane bcc(002) and in-plane bcc(200) reflections are observed for the single-crystal $Fe_{70}Co_{30}$ and $(Fe_{0.7}Co_{0.3})_{95}B_5$ films [Figs. 7(a), (b)]. In the XRD patterns measured for the $(Fe_{0.7}Co_{0.3})_{90}B_{10}$ film consisting of bcc(001) and bcc(122) variants [Fig. 7(c)], weak out-of-plane and in-plane reflections from bcc(001) variant are recognized, while reflections from bcc(122) variants are absent, since the bcc(122) reflection is forbidden. The present study shows that a combination of RHEED or pole-figure XRD with conventional out-of-plane and in-plane XRDs is effective to determine whether an Fe-Co-B film involves bcc(122) crystals in addition to bcc(001) crystal. No reflections from bcc crystals are observed in the out-of-plane and in-plane patterns measured for the amorphous $(Fe_{0.7}Co_{0.3})_{85}B_{15}$ film [Fig. 7(d)].

Figure 8 shows the out-of-plane and in-plane orientation dispersions, $\Delta\theta_{50}$ and $\Delta\theta\chi_{50}$, measured for single-crystal $(Fe_{0.7}Co_{0.3})_{100-x}B_x$ films. Here, the $\Delta\theta_{50}$ and $\Delta\theta\chi_{50}$ values are respectively the full widths at half maximum of ω- and φ-scan rocking curves measured by setting the diffraction angles of 2θ and $2\theta\chi$ at the peak angles of bcc(002) and bcc(200) reflections. The $\Delta\theta_{50}$ and $\Delta\theta\chi_{50}$ values decrease not only with increasing the

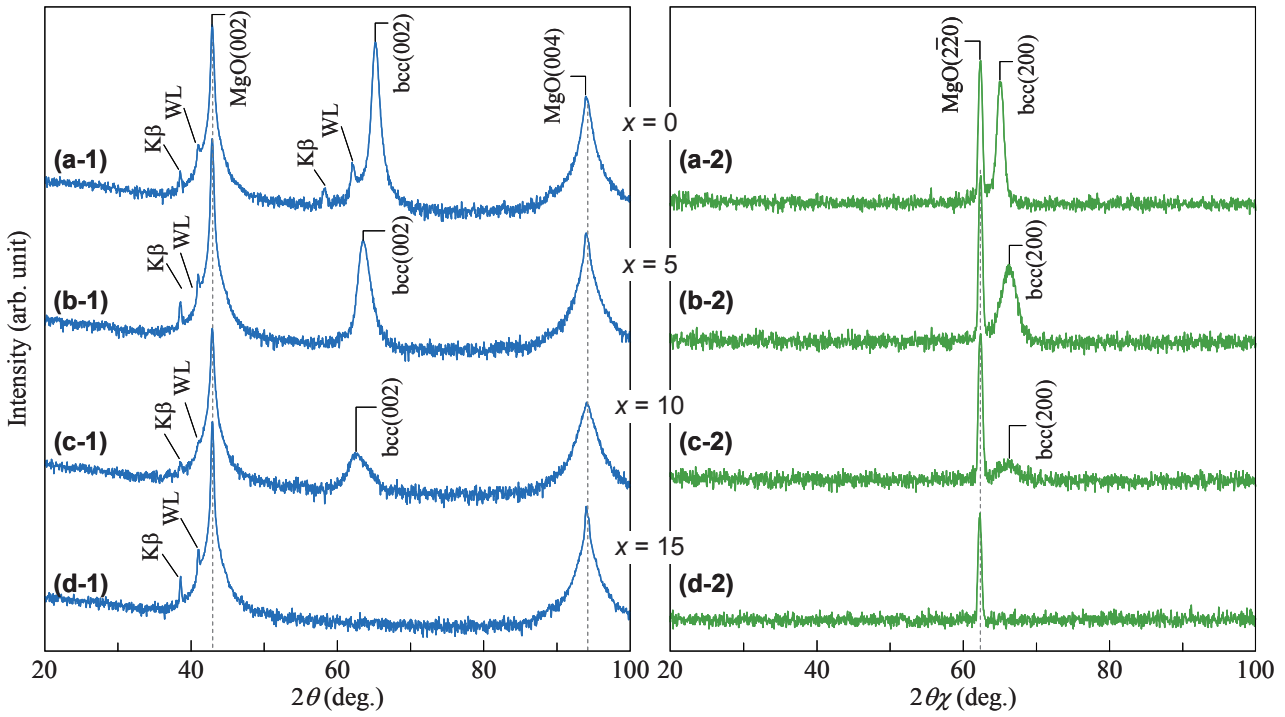

Fig. 7 (a-1)–(d-1) Out-of-plane and (a-2)–(d-2) in-plane XRD patterns measured for $(Fe_{0.7}Co_{0.3})_{100-x}B_x$ films with the B contents of (a) 0, (b) 5, (c) 10, and (d) 15 at. % deposited on MgO(001) substrates at 200 °C. The in-plane XRD patterns are measured by making the scattering vector parallel to MgO[1$\bar{1}$0]. The intensity is shown in logarithmic scale.

substrate temperature but also with decreasing the B content. The crystallographic quality is improved for an $(Fe_{0.7}Co_{0.3})_{100-x}B_x$ film with a lower B content deposited at a higher substrate temperature. The result seems to be related with the structural variation of bcc(001) single-crystal => bcc(001) and bcc(122) crystals => bcc polycrystal => amorphous.

Figure 9 shows the substrate temperature dependences of in-plane and out-of-plane lattice parameters, a and c, and the ratio, c/a, of single-crystal $Fe_{70}Co_{30}$ film. Here, the a and the c values are respectively calculated from the peak angles of bcc(002) and bcc(200) reflections by using the relations of

$$a = 2[\lambda / 2\sin(\theta\chi)_{bcc(200)}], \quad (4)$$

$$c = 2[\lambda / 2\sin(\theta)_{bcc(002)}]. \quad (5)$$

The errors are estimated by using the relationships of

$$(\Delta a) / 2 = \pm \{a\,[\cot(\theta\chi)_{bcc(200)}]\,\Delta(\theta\chi)_{bcc(200)}\} / 2, \quad (6)$$

$$(\Delta c) / 2 = \pm \{c\,[\cot(\theta)_{bcc(002)}]\,\Delta(\theta)_{bcc(002)}\} / 2. \quad (7)$$

For the film deposited at RT, the a value (0.2896 nm) is larger than the c value (0.2836 nm). The in-plane and out-of-plane lattices are respectively expanded and contracted in accommodation of the lattice mismatch of −4.2% existing at the $Fe_{70}Co_{30}$/MgO interface. With increasing the substrate temperature from RT to 200 °C, the c/a value is approaching to 1. For the substrate temperature range of 200–600 °C, the c/a value is almost kept constant at 1. The lattice deformation is relaxed by using temperatures higher than 200 °C.

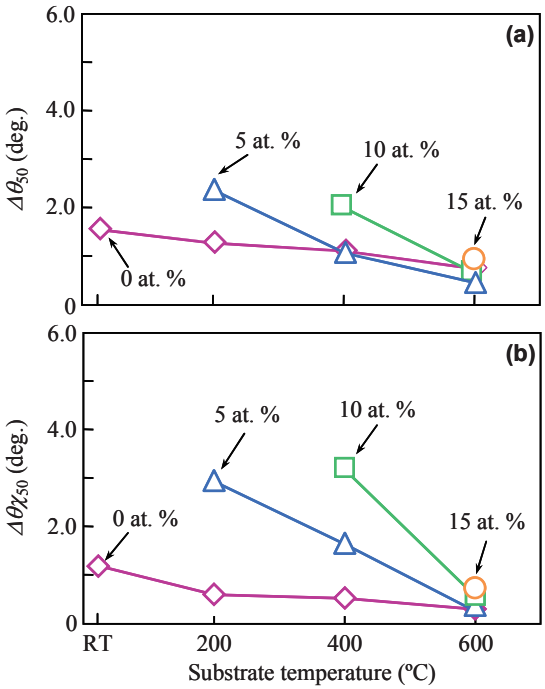

Fig. 8 Substrate temperature dependences of (a) $\Delta\theta_{50}$ and (b) $\Delta\theta\chi_{50}$ values measured for single-crystal $(Fe_{0.7}Co_{0.3})_{100-x}B_x$ films with different B contents.

Figure 10 shows the lattice parameters of single-crystal $(Fe_{0.7}Co_{0.3})_{100-x}B_x$ (x = 5–15 at. %) films.

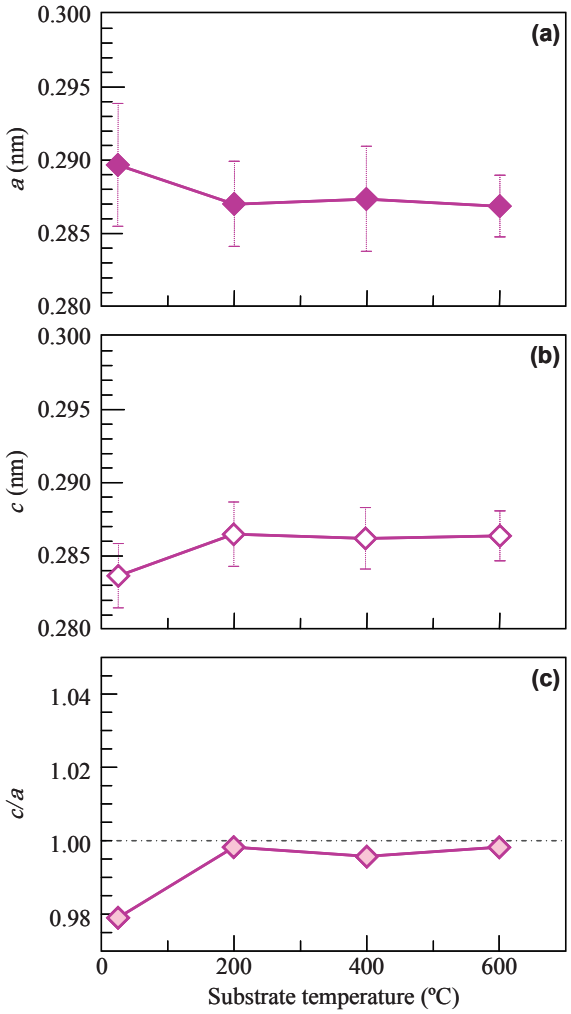

Fig. 9 Lattice parameters, (a) a, (b) c, and (c) c/a, measured for single-crystal $Fe_{70}Co_{30}$ films.

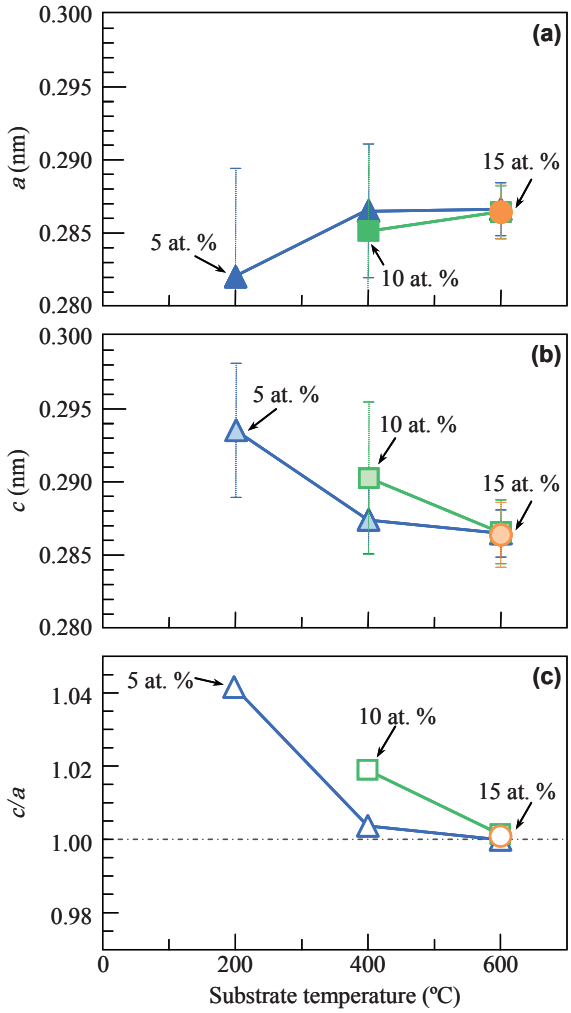

Fig. 10 Lattice parameters, (a) a, (b) c, and (c) c/a, measured for single-crystal $(Fe_{0.7}Co_{0.3})_{100-x}B_x$ (x = 5–15 at. %) films.

For the $(Fe_{0.7}Co_{0.3})_{95}B_5$ film deposited at 200 °C, the a value (0.2818 nm) is smaller than the c value (0.2935 nm). The in-plane and out-of-plane lattices are respectively contracted and expanded, though there exists the mismatch with minus sign at the film/substrate interface. The crystal lattice is deformed along the perpendicular direction by addition of B atoms. With increasing the substrate temperature from 200 to 600 °C, the c/a value of $(Fe_{0.7}Co_{0.3})_{95}B_5$ film decreases from 1.042 to 1.000. The lattice strain decreases with increasing the substrate temperature, similar to the case of $Fe_{70}Co_{30}$ film. The c/a value (1.019) of $(Fe_{0.7}Co_{0.3})_{90}B_{10}$ film deposited at 400 °C is larger than that (1.004) of $(Fe_{0.7}Co_{0.3})_{95}B_5$ film deposited at 400 °C. A higher B content is apparently enhancing the lattice deformation.

3.3 Surface morphology and magnetic properties

Figure 11 shows the AFM image observed for $Fe_{70}Co_{30}$ films deposited at 200–600 °C. The film growth on MgO substrate seems to follow Volmer-Weber[21] (island-like growth) mode. The film deposited at 200 °C

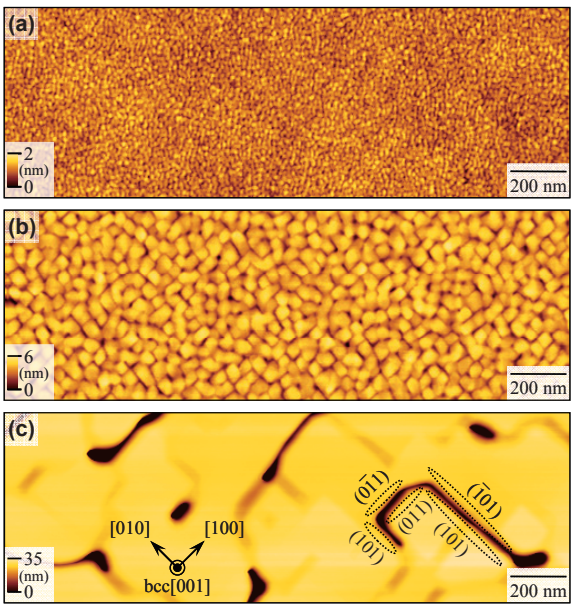

Fig. 11 AFM images observed for $Fe_{70}Co_{30}$ films deposited on MgO(001) substrates at (a) 200, (b) 400, and (c) 600 °C.

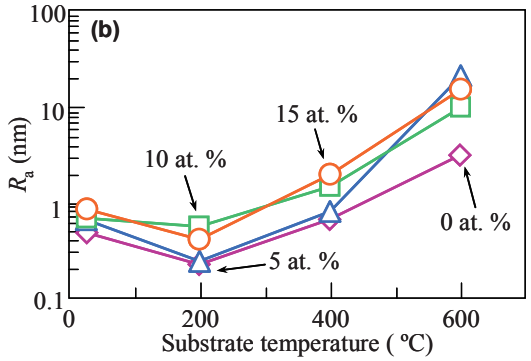

Fig. 12 Substrate temperature dependences of R_a values measured for $(Fe_{0.7}Co_{0.3})_{100-x}B_x$ films with different B contents.

has a flat surface with the arithmetical mean roughness, R_a, of 0.2 nm [Fig. 11(a)]. When the substrate temperature is increased up to 400 °C, an island-like surface involving side bcc{110} facets is recognized [Fig. 11(b)]. The orientations of facets were estimated from the cross-sectional profiles of the AFM images (not shown here). With further increasing the substrate temperature to 600 °C, the island size drastically increases [Fig. 11(c)]. Migration and clustering of deposited atoms are promoted by employing a higher substrate temperature. Figure 12 summarizes the substrate temperature dependences of R_a values measured for $(Fe_{0.7}Co_{0.3})_{100-x}B_x$ films. Similar tendencies are observed, even though the B contents are different.

Figure 13 shows the in-plane magnetization curves of single-crystal $Fe_{70}Co_{30}$ films deposited at different temperatures measured by applying the magnetic field along bcc[100] or bcc[110]. The films are easily magnetized when the magnetic field is applied along bcc[100], while the magnetization curves measured along bcc[110] saturate at higher magnetic fields. There were no clear differences in the hysteresis loops measured along bcc[100] and bcc[010] and measured along bcc[110] and bcc[1$\bar{1}$0] (not shown here). Therefore, the films show four-fold symmetries in in-plane magnetic anisotropies, which are reflecting the

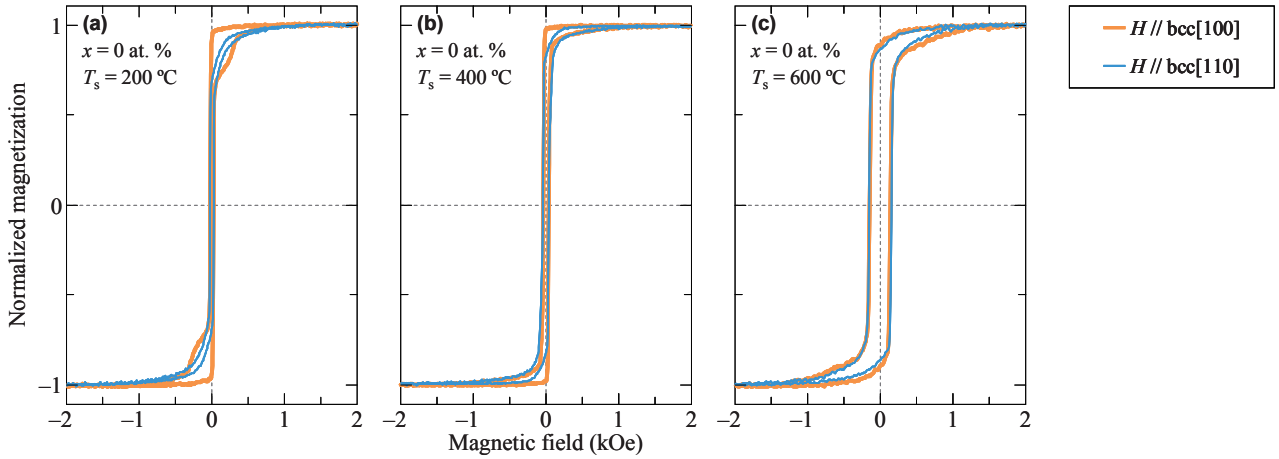

Fig. 13 In-plane magnetization curves measured for single-crystal $Fe_{70}Co_{30}$ films formed at (a) 200, (b) 400, and (c) 600 °C. The magnetic field is applied along bcc[100] or bcc[110].

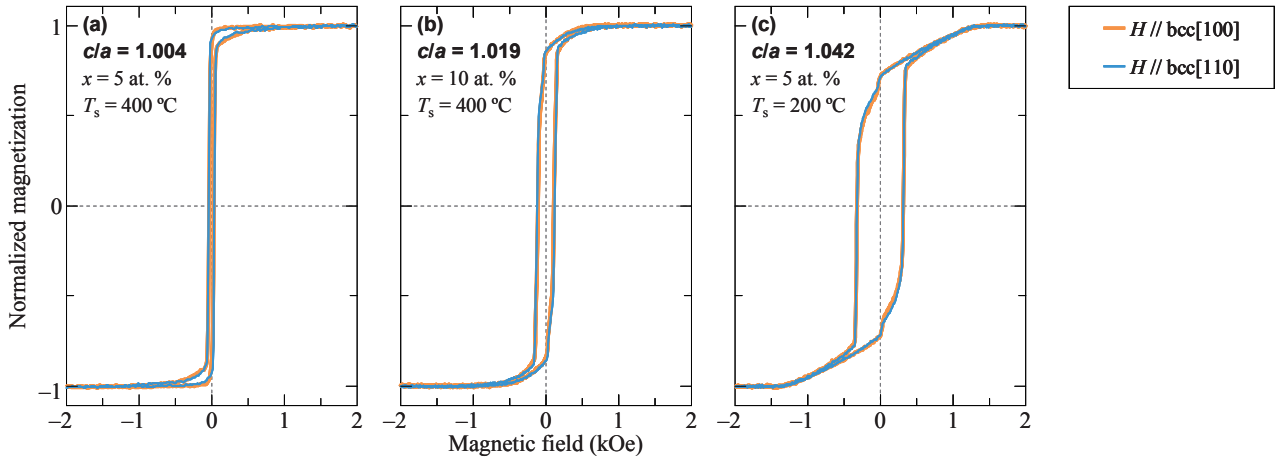

Fig. 14 In-plane magnetization curves measured for single-crystal $(Fe_{0.7}Co_{0.3})_{100-x}B_x$ films with the c/a ratios of (a) 1.004, (b) 1.019, (c) 1.042. The magnetic field is applied along bcc[100] or bcc[110].

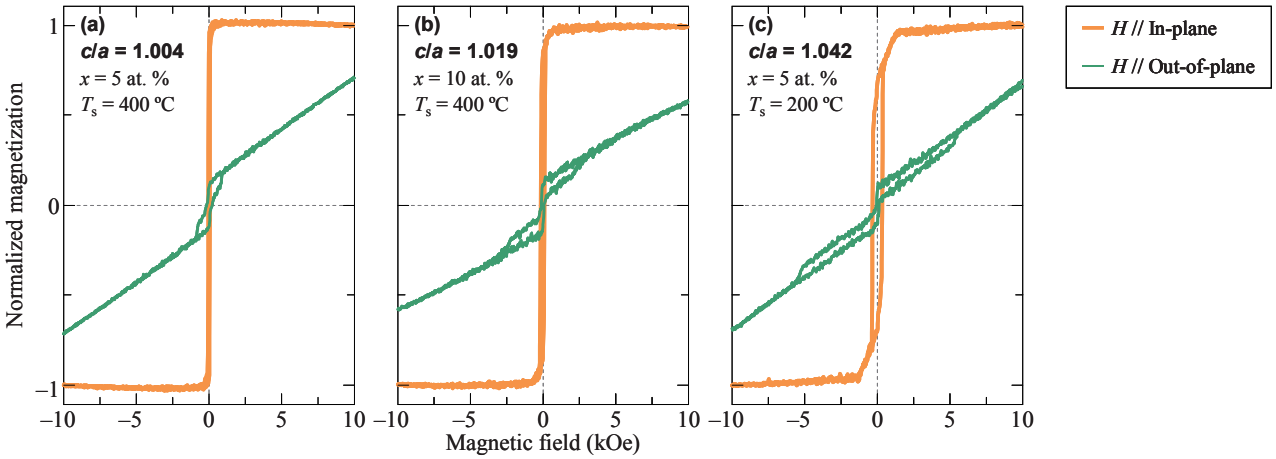

Fig. 15 Out-of-plane and in-plane magnetization curves measured for single-crystal $(Fe_{0.7}Co_{0.3})_{100-x}B_x$ films with the *c*/*a* ratios of (a) 1.004, (b) 1.019, and (c) 1.042.

magnetocrystalline anisotropy of bulk $Fe_{70}Co_{30}$ alloy with the easy magnetization axes of bcc<100>. The in-plane anisotropy decreases as the substrate temperature increases. The magnetic anisotropy seems to be influenced not only by the magnetocrystalline anisotropy but also by the shape anisotropy caused by the surface undulation, which is more enhanced by using a higher substrate temperature. With increasing the substrate temperature from 200 to 600 °C, the coercivity of hysteresis curve measured along bcc[100] increases from 2.5 to 150 Oe. Domain wall motion seems to be suppressed by the crevasses existing between islands, as shown in the AFM image of Fig. 11(c).

Figure 14 shows the in-plane magnetization curves of single-crystal $(Fe_{0.7}Co_{0.3})_{100-x}B_x$ films with the *c*/*a* ratios of 1.004, 1.019, and 1.042 whose B contents are 5, 10, and 5 at. % and whose formation temperatures are 400, 400, and 200 °C, respectively. Although the films are composed of bcc(001) single-crystal, almost isotropic in-plane curves are observed. As the *c*/*a* ratio increases from 1.004 to 1.042, the coercivity increases from 30 to 320 Oe, whereas the remnant magnetization, M_r/M_s, decreases from 0.923 to 0.718. The result indicates that perpendicular magnetic anisotropies have been also induced in the strained $(Fe_{0.7}Co_{0.3})_{100-x}B_x$ single-crystal films, similar to the cases of previous studies[9–16]. Figure 15 shows the out-of-plane and in-plane hysteresis loops measured for the $(Fe_{0.7}Co_{0.3})_{100-x}B_x$ films. The films show weak perpendicular magnetic anisotropies. The perpendicular magnetic anisotropy seems to have been slightly enhanced with increasing the *c*/*a* ratio. The magnetic properties are apparently influenced by the lattice deformation.

4. Conclusion

$(Fe_{0.7}Co_{0.3})_{100-x}B_x$ alloy films are prepared by sputter deposition on MgO(001) substrates by varying the B content from 0 to 15 at. % and by varying the substrate temperature from RT to 600 °C. The detailed structural properties are investigated by RHEED and XRD. Single-crystal $(Fe_{0.7}Co_{0.3})_{100-x}B_x$ films with the B contents of 0, 5, 10, and 15 at. % are formed at temperatures higher than RT, 200 °C, 400 °C, and 600 °C, respectively. The crystallographic orientation relationship is bcc-$(Fe_{0.7}Co_{0.3})_{100-x}B_x$(001)[110] ‖ MgO(001)[100]. As the B content increases and the substrate temperature decreases, the structure varies in the order of bcc(001) single-crystal => a mixture of bcc(001) and bcc(122) crystals => polycrystal => amorphous. The lattice of single-crystal $Fe_{70}Co_{30}$ film is expanded along the in-plane direction in accommodation of the mismatch existing at the $Fe_{70}Co_{30}$(001)/MgO(001) interface. On the contrary, the lattices of single-crystal $(Fe_{0.7}Co_{0.3})_{100-x}B_x$ (x = 5–15 at. %) films are expanded along the perpendicular direction. The $Fe_{70}Co_{30}$ films show in-plane magnetic anisotropies reflecting the magnetocrystalline anisotropy of bulk $Fe_{70}Co_{30}$ crystal, whereas the $(Fe_{0.7}Co_{0.3})_{100-x}B_x$ films show weak perpendicular magnetic anisotropies, which are possibly caused by an influence of lattice strain along the perpendicular direction.

Acknowledgement A part of this work was supported by Chuo University Grant for Special Research.

References

1) S. S. P. Parkin, C. Kaiser, A. Panchula, P. M. Rice, B. Hughes, M. Samant, and S. H. Yang: *Nature Mater.*, **3**, 862 (2004).
2) S. Yuasa, T. Nagahama, A. Fukushima, Y. Suzuki, and K. Ando: *Nature Mater.*, **3**, 868 (2004).
3) Y. Asai, M. Ohtake, T. Kawai, and M. Futamoto: *J. Korean Phys. Soc.*, **63** 733 (2013).
4) L. Reichel, L. Schultz, D. Pohl, S. Oswald, S. Fähler, M. Werwiński, A. Edström, E. K. Delczeg-Czirjak, and J. Rusz: *J. Phys.: Condens. Matter*, **27** 476002 (2015).
5) Y. H. Ghang, S. W. Yung, T. S. Chin, and M. P. Hung: *Jpn. J. Appl. Phys.*, **26**, 2041 (1987).
6) J. Yu, C. Chang, D. Karns, G. Ju, Y. Kubota, W. Eppler, C.

Brucker, and D. Weller: *J. Appl. Phys.*, **91**, 8357 (2002).
7) K. Lee, J. J. Sapan, S. H. Kang, and E. E. Fullerton: *J. Appl. Phys.*, **109**, 123910 (2011).
8) N. Sato, R. M. White, and S. X. Wang: *J. Appl. Phys.*, **108**, 152405 (2016).
9) W. B. Person: *A Handbook of Lattice Spacings and Structures of Metals and Alloys* (Pergamon Press, London, New York, Los Angeles, Paris, 1958) pp. 504–505.
10) J. Yamashita and S. Asano: *J. Phys. Soc. Jpn.*, **52**, 3506 (1983).
11) K. Matsubara, M. Ohtake, K. Tobari, and M. Futamoto: *Thin Solid Films*, **519**, 8299 (2011).
12) T. Nishiyama, K. Shikada, M. Ohtake, F. Kirino, and M. Futamoto: *J. Magn. Soc. Jpn.*, **34**, 5 (2010).
13) J. A. Venable: *Introduction to Surface and Thin Film Process* (Cambridge Univ. Press, New York, 2000) pp. 145–147.
14) T. Burkert, L. Nordström, O. Eriksson, and O. Heinonen: *Phys. Rev. Lett.*, **93**, 027203 (2004).
15) Y. Kota and A. Sakuma: *J. Magn. Soc. Jpn.*, **37**, 17 (2013).
16) G. Andersson, T. Burkert, P. Warnicke, M. Björck, B. Sanyal, C. Chacon, C. Zlotea, L. Nordström, P. Nordblad, and O. Eriksson: *Phys. Rev. Lett.*, **96**, 037205 (2006).
17) A. Winkelmann, M. Przybylski, F. Luo, Y. Shi, and J. Barthel: *Phys. Rev. Lett.*, **96**, 257205 (2006).
18) F. Yildiz, M. Przybylski, X. -D. Ma, and J. Kirschner: *Phys. Rev. B*, **80**, 064415 (2009).
19) B. Lao, J. W. Jung, and M. Sahashi: *IEEE Trans. Magn.*, **50**, 2008704 (2014).
20) H. Oomiya, B. Wang, S. Yoshida, T. Kataguchi, K. Takahashi, S. Kanatani, L. Zhang, L. Liu, T. Hasegawa, K. Hayasaka, S. Saito, N. Inami, T. Ueno, K. Ono, and S. Ishio: *J. Phys. D: Appl. Phys.*, **48**, 475003 (2015).
21) S. Ishio, T. Hasegawa, S. Yoshida, S. Kanatani, K. Takahashi, K. Kumagaya, and M. Hirao: *Magnetics Jpn.*, **12**, 21 (2017).

Received Apr. 4, 2017; Accepted Jun. 10, 2017

Journal of the Magnetics Society of Japan

Vol. 41 No. 5 (通巻第 293 号) 2017 年 9 月 1 日発行

Vol. 41 No. 5 Published Sep 1, 2017
by the Magnetics Society of Japan
Tokyo YWCA building Rm207, 1–8–11 Kanda surugadai, Chiyoda-ku, Tokyo 101–0062
Tel. +81–3–5281–0106 Fax. +81–3–5281–0107

Printed by JP Corporation Co., Ltd.
2–3–36, Minamikase, Saiwai-ku, Kanagawa 212–0055
Advertising agency: Kagaku Gijutsu-sha

発行：（公社）日本磁気学会 101–0062 東京都千代田区神田駿河台 1–8–11 東京YWCA会館 207 号室
製作：ジェイピーコーポレーション 212–0055 神奈川県川崎市幸区南加瀬 2–3–36 Tel.（044）571–5815
広告取扱い：科学技術社 111–0052 東京都台東区柳橋 2–10–8 武田ビル 4F Tel.（03）5809–1132